bioRxiv preprint doi: https://doi.org/10.1101/813188; this version posted October 21, 2019. The copyright holder for this preprint (which was not certified by peer review) is the author/funder, who has granted bioRxiv a license to display the preprint in perpetuity. It is made available under aCC-BY-NC 4.0 International license.

Quantitative properties of a feedback circuit predict frequency-dependent pattern separation

Running Title: Feedback inhibition in dentate gyrus

Oliver Braganza[1*], Daniel Müller-Komorowska[1,2], Tony Kelly[1] and Heinz Beck[1,3 *]

[1]Institute for Experimental Epileptology and Cognition Research, University of Bonn

[2]International Max Planck Research School for Brain and Behavior, University of Bonn

[3]Deutsches Zentrum für Neurodegenerative Erkrankungen e.V., Bonn, Germany

* Correspondence should be addressed to:

Heinz Beck

Institute for Experimental Epileptology and Cognition Research, University of Bonn

Sigmund-Freud Str. 25

53105 Bonn

Tel.: 0228 6885 270

Fax: 0228 6885 294

e-mail: Heinz.beck@ukbonn.de

Oliver Braganza (Lead Contact)

Institute for Experimental Epileptology and Cognition Research, University of Bonn

Sigmund-Freud Str. 25

53105 Bonn

bioRxiv preprint doi: https://doi.org/10.1101/813188; this version posted October 21, 2019. The copyright holder for this preprint (which was not certified by peer review) is the author/funder, who has granted bioRxiv a license to display the preprint in perpetuity. It is made available under aCC-BY-NC 4.0 International license.

Tel.: 0228 6885 157

Fax: 0228 6885 294

e-mail: oliver.braganza@ukbonn.de

Pages: 67

Figures: 6 (+11 Suppl.)

Tables: (2 Suppl.)

Abstract: 159 words; Introduction: 475 words; Results: 4366 words; Discussion: 1207 words

bioRxiv preprint doi: https://doi.org/10.1101/813188; this version posted October 21, 2019. The copyright holder for this preprint (which was not certified by peer review) is the author/funder, who has granted bioRxiv a license to display the preprint in perpetuity. It is made available under aCC-BY-NC 4.0 International license.

Abstract

Feedback inhibitory motifs are important for pattern separation in several species. How feedback circuits implement pattern separation of biologically plausible, temporally structured input in mammals is poorly understood, partly because the spatiotemporal organization of the net output of these circuits has not been characterized. We have quantitatively determined key properties of *net* feedback inhibition in the mouse dentate gyrus, a region critically involved in pattern separation. Feedback inhibition is recruited steeply with a low dynamic range (0 to 4% of active GCs), and with a non-uniform spatial profile. Additionally, net feedback inhibition shows frequency-dependent facilitation, driven by strongly facilitating mossy fiber inputs. Computational analyses show a significant contribution of the feedback circuit to pattern separation of theta modulated inputs, even within individual theta cycles. Moreover, pattern separation was selectively boosted at gamma frequencies, in particular for highly similar inputs. This effect was highly robust, suggesting that frequency dependent pattern separation is a key feature of the feedback inhibitory microcircuit.

bioRxiv preprint doi: https://doi.org/10.1101/813188; this version posted October 21, 2019. The copyright holder for this preprint (which was not certified by peer review) is the author/funder, who has granted bioRxiv a license to display the preprint in perpetuity. It is made available under aCC-BY-NC 4.0 International license.

Introduction

Efficiently discriminating similar percepts or experiences is a central capability common to invertebrate and vertebrate species. In general terms, such discrimination can be achieved by decreasing the overlap in representations by neuronal ensembles between input and output patterns, a process termed 'pattern separation' [1–4]. Numerous studies have proposed cellular and circuit mechanisms that could support this computation. For instance, sparse divergent inputs and specialized intrinsic properties are thought to generally contribute [1,5,6]. Another common feature of most of these models and experimental studies is a critical role of feedback inhibition [4,6]. Feedback circuits can i) implement direct competition between active cells through lateral inhibition and can ii) integrate information about the actual global activity level in a population allowing efficient normalization [7–9]. Indeed, in the insect olfactory system a critical role of such a circuit has been causally demonstrated [10,11]

In mammals, substantial evidence points towards a role of the hippocampal dentate gyrus (DG) for pattern separation during memory formation and spatial discrimination [12–20]. The DG is thought to subserve this task by converting different types of inputs to sparse, non-overlapping activity patterns of granule cells (GCs). However, in contrast to the insect olfactory system, the DG feedback circuit is extremely complex, comprising numerous interconnected interneuron types (Supplementary Table 1)[21–39]. For instance, interneurons subserving feedback inhibition are also incorporated into circuits mediating feedforward inhibition[32,35,40] and disinhibition [21,29]. This makes it difficult to predict the *net* inhibition arising from GC activity.

We reasoned that to assess if feedback inhibition is indeed suitable for the purpose of pattern separation in the DG, it is necessary to determine how efficiently the activity of sparse GC ensembles recruits *net* inhibition, i.e. the dynamic range and gain of the feedback inhibitory microcircuit. It is furthermore necessary to quantify the spatial and temporal properties of the elicited inhibition, in order to investigate its impact on biologically plausible,

bioRxiv preprint doi: https://doi.org/10.1101/813188; this version posted October 21, 2019. The copyright holder for this preprint (which was not certified by peer review) is the author/funder, who has granted bioRxiv a license to display the preprint in perpetuity. It is made available under aCC-BY-NC 4.0 International license.

temporally structured input. For instance, the DG shows prominent theta oscillations during exploration and distinctive slow-gamma activity during associative memory encoding [41–44]. Importantly, both sparsity and temporal oscillations will critically affect a proposed pattern separation function. For instance, feedback inhibition must by definition occur with a delay, a property frequently abstracted away in computational models [45,46], but potentially critical during oscillatory activity.

Here, we combine patch-clamp recordings, multiphoton imaging and optogenetics to provide a first quantitative, empirical description of the *net* input-output function of a feedback inhibitory microcircuit. This includes the spatiotemporal organization of *net* feedback inhibition elicited by a spatially restricted GC population and the *net* short term dynamics within the feedback microcircuit. Finally, we integrate our data into a biophysically realistic computational model and probe its ability to perform pattern separation. We find a moderate feedback inhibition mediated pattern separation effect during theta modulated input but a substantial separation, particularly of highly similar inputs, during gamma oscillations.

bioRxiv preprint doi: https://doi.org/10.1101/813188; this version posted October 21, 2019. The copyright holder for this preprint (which was not certified by peer review) is the author/funder, who has granted bioRxiv a license to display the preprint in perpetuity. It is made available under aCC-BY-NC 4.0 International license.

Results

Input-output relation of the feedback inhibitory microcircuit

We reasoned that the ultimately relevant parameter for the putative pattern separation effect of feedback inhibition is the *net* inhibition arriving at GCs. We therefore treated the feedback microcircuit as a black-box striving to relate only its *net* input (fraction of GCs active) to its *net* output (feedback inhibition in GCs). To this end we antidromically recruited feedback inhibitory circuits, while simultaneously recording GC inhibition and population activity (see schematic in **Fig. 1A**). Electrical stimulation reliably evoked graded IPSCs in dentate GCs, that increased with stimulation strength (maximal amplitude of 324.1±99.2 pA, n=8; **Fig. 1B**). Feedback IPSCs were completely blocked by 10µM GABAzine (to 1.5±0.9%, n=7 cells, P(df=6, t=117.4)<.001, one-sided t-test), as expected (**Fig. 1C)**. To ascertain that IPSCs were mediated by synaptically activated interneurons rather than interneurons directly recruited by electrical stimulation, we only included slices where inhibition was successfully blocked by glutamatergic antagonists (25µM CNQX and 50µM D-APV, 8 of 21 experiments, **Fig. 1C**). We also tested if inhibition of glutamate release from mossy fibers, which can be specifically achieved via mGluR2/3 activation by DCG-IV[47,48], reduces feedback IPSCs. Indeed, we found that IPSCs were reduced to 16.3±6.1% by 0.5 µM DCG-IV (n=4 cells, P(df=3, t=13.73)<.001, one-sided t-test, **Fig. 1C**).

In order to relate the measured IPSCs to the fraction of GCs activated by a given stimulation strength, we used population Ca^{2+} imaging with multibeam two-photon microscopy (**Fig. 1A,** see Methods). After bolus-loading GCs with the Ca^{2+} indicator OGB-1-AM (see Methods), antidromic stimulation caused action potential associated Ca^{2+} elevations in a subset of GCs (**Fig. 1D,** transients indicated by *). Before quantifying population activity, we verified the reliable detection of single action potentials under our conditions using simultaneous cell-attached recordings from dentate GCs (**Fig. 1E, Supplementary Fig. 1**). Briefly, cells were differentiated into true responders or non-responders on the basis of cell-attached recordings (**Fig. 1E, F**; responders green, non-responders grey). A histogram of the peak ΔF/F of non-

bioRxiv preprint doi: https://doi.org/10.1101/813188; this version posted October 21, 2019. The copyright holder for this preprint (which was not certified by peer review) is the author/funder, who has granted bioRxiv a license to display the preprint in perpetuity. It is made available under aCC-BY-NC 4.0 International license.

responders upon a single stimulus was fitted with a Gaussian (**Fig. 1F** right, grey dots, grey bars, n=33) and the threshold set to the quadruple standard deviation of this fit (0.94% ΔF/F, dashed line in **Fig. 1F**). We estimated that this threshold would yield approximately equal numbers of false positives and false negatives (**Supplementary Fig. 1F**). We additionally controlled for possible errors through variable dye loading and the overestimation of the active cell-fraction through accidental detection of adjacent active cells (**Supplementary Fig. 1G, H**, respectively).

Orientation of hippocampal slices may be a critical feature in determining the extent of feedback connectivity. We therefore systematically assessed the magnitude of feedback activation of GCs using imaging in slices obtained from different dorso-ventral levels of the hippocampus (see inset of **Fig. 1 G**). We found a clear connectivity maximum within horizontal slices obtained at a distance of ~1750 µm from the temporal pole (**Fig. 1G,H**)[49]. In these and all following experiments we therefore used exclusively slices obtained at 1400-2100 µm from the temporal pole, where the orientation of hippocampal slices matches the orientation of mossy fibers.

Combining the IPSC recordings with population Ca^{2+} imaging allowed us to probe the input-output relationship of the feedback inhibitory microcircuit. Inhibition was recorded in a GC within or immediately adjacent to the imaging field, and stimulation strength was increased gradually (**Fig. 1I**). The IPSC saturated at 300µA stimulation strength, where the mean active cell fraction was 2.2±0.7% and the mean IPSC reached 93.1±3.4% of the maximal IPSC (**Fig. 1I**, **J,** n=20 for imaging, n=8 for IPSCs including 6 slices with both). Plotting the IPSC magnitude vs. the cell fraction showed that the magnitude of feedback inhibition rises steeply, reaching ~90% with less than 3% of GCs active and complete saturation at 3.7±1.7% of cells (**Fig. 1K**).

bioRxiv preprint doi: https://doi.org/10.1101/813188; this version posted October 21, 2019. The copyright holder for this preprint (which was not certified by peer review) is the author/funder, who has granted bioRxiv a license to display the preprint in perpetuity. It is made available under aCC-BY-NC 4.0 International license.

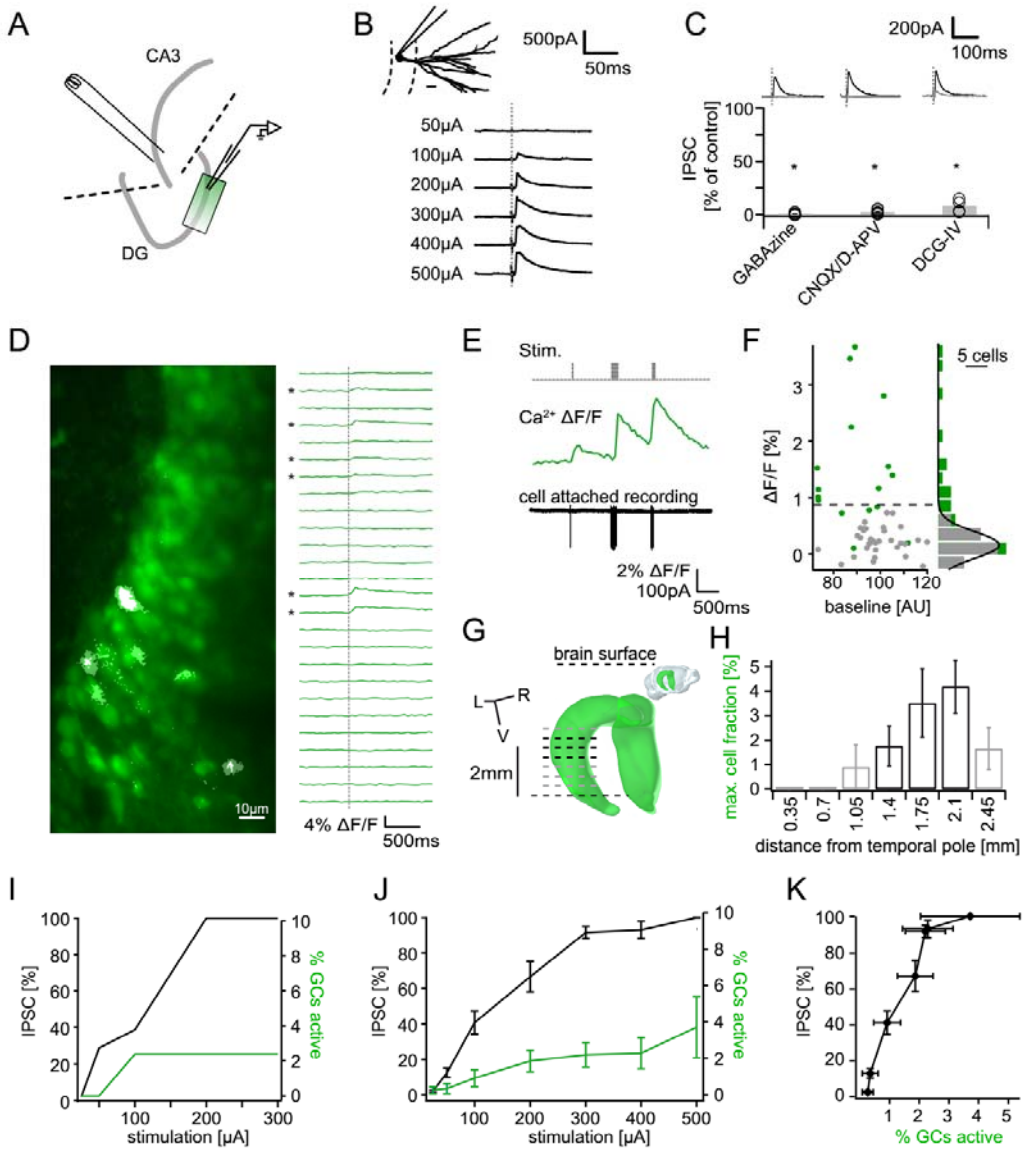

Fig. 1, Recruitment of feedback inhibition assessed using population Ca^{2+} imaging. Combined population Ca^{2+} imaging and IPSC recordings of GCs during antidromic electrical stimulation. **A)** Schematic illustration of the experimental setup. Dashed lines represent cuts to sever CA3 backprojections. **B)** Top: reconstruction of the dendritic tree of a representative GC. Bottom: Feedback IPSC at increasing stimulation strength during stratum lucidum stimulation. **C)** IPSCs were completely blocked by GABAzine and CNQX + D-APV and largely by DCG-IV. **D)** left: overlay of exemplary OGB1-AM loaded GC population (green) with a ΔF/F map (white). right: traces of ΔF/F over time of a subpopulation of cells depicted on the left. **E)** Simultaneous cell attached recording and calcium imaging to measure the action potential induced somatic calcium transient amplitude. **F)** Scatterplot and histogram of the calcium fluorescence peaks of cells which either did (green) or did not (grey) fire action potentials, as assessed by cell attached recordings. **G)** Illustration of the anatomical localization of maximum connectivity plane slices. Short black dashed lines indicate depth at which the slice plane is aligned to the dorsal brain surface. **H)** Antidromic stimulation elicited Ca^{2+} transients primarily at this depth (black bars). **I)** Normalized IPSC amplitude and activated cell fraction both increase with increasing stimulation strength (example from a single slice). **J)** Summary of all slices **K)** Summary data plotted to show the increase of inhibition as a function of the active GC fraction.

bioRxiv preprint doi: https://doi.org/10.1101/813188; this version posted October 21, 2019. The copyright holder for this preprint (which was not certified by peer review) is the author/funder, who has granted bioRxiv a license to display the preprint in perpetuity. It is made available under aCC-BY-NC 4.0 International license.

Optogenetic quantification of the recruitment of feedback inhibition

These experiments yielded a first quantitative estimate of the input-output relation of the feedback-inhibitory microcircuit in the DG. We then decided to verify these findings using an alternative method, which allowed spatially controlled and less synchronous GC activation. Mice selectively expressing ChR2$^{(H134R)}$-eYFP in GCs were created by crossing Prox1-Cre mice with Ai32-mice (**Fig. 2A**, see methods). Focal optogenetic stimulation was achieved through a laser coupled into the microscope light path, yielding an 8 µm stimulation spot **(Fig. 2B)**. Brief (20 ms, 473 nm) light pulses within the molecular layer approximately 40 µm from the dentate GC layer elicited reliable IPSCs in GCs **(Fig. 2C)**. Increasing the light intensity evoked larger IPSCs that showed clear saturation (**Fig. 2C, D,** Power=7 AU corresponding to 1.7 mW, see Methods). Inhibition was completely blocked by combined application of 40µM CNQX and 50µM D-APV (**Fig. 2E**, n=9), confirming that it is recruited via glutamatergic collaterals. The maximal IPSC amplitude obtained optically vs. electrically in experiments in which both stimulations were performed were similar (**Fig. 2F**, paired t-test, P(df=3, t=1.568)=.2148, n=4), indicating that similar maximal inhibition is recruited despite the differences in the activated GC population (distributed vs local; synchronous vs. less synchronous).

In order to relate feedback inhibition to the underlying GC activity levels, we performed systematic cell attached recordings of GCs in the same slices in which inhibition was recorded (~2 cells per slice, **Supplementary Fig. 2**). Briefly, we recorded the spatial firing probability distribution in response to focal stimulation for each laser power. We then estimated the mean firing probability of GCs throughout the section, which is equivalent to the expected active GC fraction, by incorporating measurements of the light intensity distribution throughout the slice (**Fig. 2G**, black). We additionally estimated an upper and lower bound by assuming either no decay of firing probability with slice depth or isometric decay (**Fig. 2G,** grey dashed lines). Combining the input-output relations of IPSCs **(Fig. 2D)** and the estimated active cell fraction **(Fig. 2G)** again revealed that inhibition is recruited steeply, saturating when approximately 4% of GC are active **(Fig. 2H).** Importantly, the

bioRxiv preprint doi: https://doi.org/10.1101/813188; this version posted October 21, 2019. The copyright holder for this preprint (which was not certified by peer review) is the author/funder, who has granted bioRxiv a license to display the preprint in perpetuity. It is made available under aCC-BY-NC 4.0 International license.

resulting recruitment function of inhibition is unlikely to be affected by voltage escape errors (**Supplementary Fig. 3**). This is because such errors scale linearly with synaptic conductance and will thus affect the absolute but not the relative amplitude of the somatically measured IPSC. Next, we compared the focal light activation with global activation via a light fiber positioned over the surface of the slice (with powers up to 50 mW, **Fig. 2I**). Under global stimulation all cells tested fired APs with 100% reliability and independent of location, even though focal stimulation in direct proximity to the cell led to much lower maximal firing probabilities (**Fig. 2I, middle**, 100.0±0.0 versus 31.2±7.1% respectively, paired t-test, P(df=7, t=9.74)<.001, n=8). At the same time, the maximal IPSC amplitude did not increase further upon global stimulation (**Fig. 2I, right**, 356.9±76.2 versus 344.3±77.5 pA, paired t-test, P(df=9, t=1.112)=.29, n=10). This implies that additional activation of remote GCs cannot recruit interneurons beyond those activated by local GC populations. Thus the recruitment of feedback inhibition in the DG is steep, with a dynamic range tuned to sparse populations of GCs (up to 3-4% of cells).

Lower limit of feedback recruitment

Previous work has addressed the lower limit of the recruitment of feedback inhibition in various cortical areas [50–53]. The authors report the ability of even a single principal cell to activate feedback inhibitory interneurons and a supralinear increase of inhibition as the second and third principal cells are co-activated [50]. Given our findings so far we asked whether single GCs might also suffice to elicit feedback inhibition in the DG. To this end we performed dual patch clamp recordings and elicited short trains of ten action potentials at 100 Hz in one cell while monitoring inhibition in the other (**Supplementary Fig. 4,** n=15). However, in contrast to the neocortex [50,52] and area CA3 [51], we did not find single GC-induced feedback inhibition in any of these experiments, consistent with a recent large scale study reporting that such connections are extremely sparse (0.124%) [22].

bioRxiv preprint doi: https://doi.org/10.1101/813188; this version posted October 21, 2019. The copyright holder for this preprint (which was not certified by peer review) is the author/funder, who has granted bioRxiv a license to display the preprint in perpetuity. It is made available under aCC-BY-NC 4.0 International license.

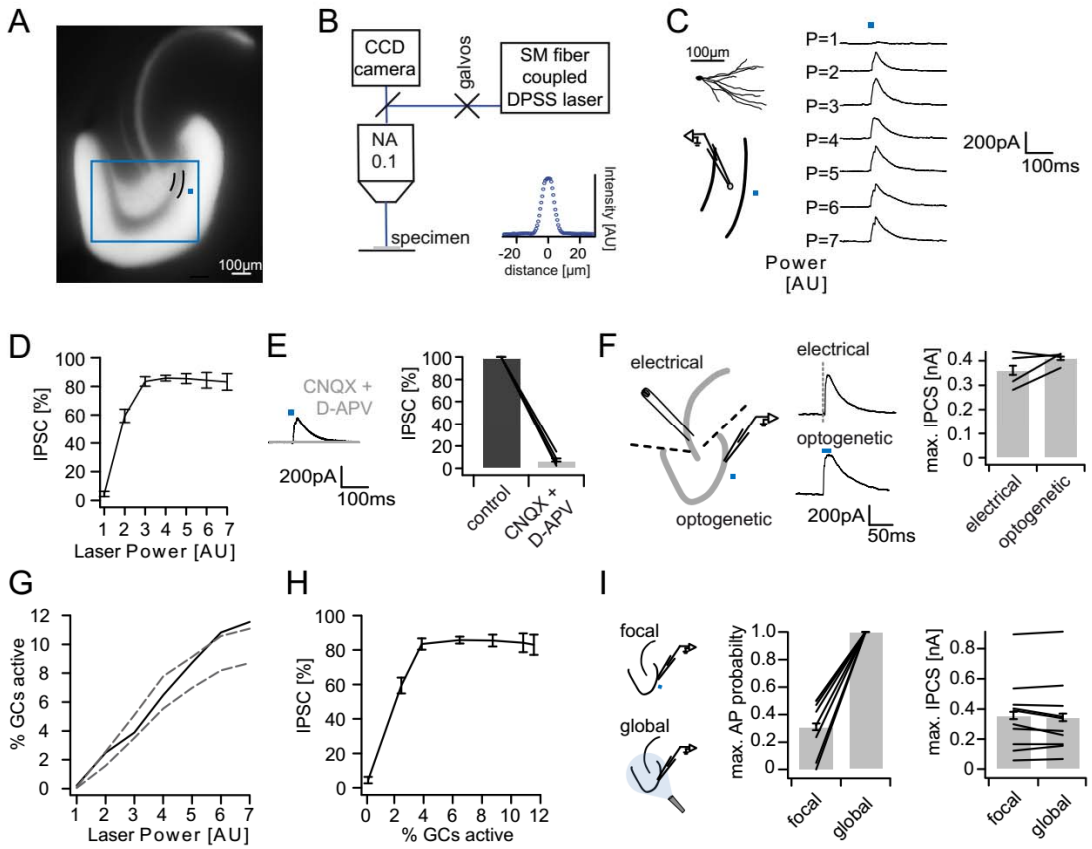

Fig. 2, Recruitment of feedback inhibition assessed optogenetically. A) EYFP fluorescence in dentate GCs of Prox1/ChR2(H134R)-EYFP transgenic mice. The field of view for rapid focal optogenetic stimulation is indicated by a blue square. A typical stimulation site approx. 40 µm from the GC layer (two short black lines) is indicated by a blue dot. **B)** Schematic of the microscope setup used to achieve spatially controlled illumination. The inset shows the intensity profile of the laser spot. **C) Top left,** reconstruction of an Alexa594 filled GC. **Left,** illustration of optical stimulation. **Right,** IPSCs following 20ms light pulses at increasing laser power (P = 1 to 7 AU). Each trace represents an average of 3 trials. **D)** Summary of IPSC amplitudes from cells in the superior blade (n=7 cells). IPSC amplitudes were normalized to the maximum amplitude within each cell. **E)** Optogenetically elicited IPSCs are abolished by glutamatergic blockers (40µM CNQX + 50µM D-APV, n=9). **F) Left,** Schematic of focal optical and electrical stimulation. Dashed lines indicate cuts to sever CA3 backprojections. **Middle,** Example traces for IPSCs following electrical or focal optogenetic stimulation. **Right,** maximal IPSC amplitude for the two stimulation paradigms (361±37 vs. 410±13 pA for electrical and optogenetic stimulation respectively, paired t-test, p=0.28, n=4) **G)** The optogenetically activated GC fraction responsible for recruiting the IPSC at the respective laser powers was estimated from systematic cell attached recordings (see Fig. S1 for details). The best estimate (black) incorporates measurements of the 3D light intensity profile in the acute slice. Upper and lower bounds were estimated by assuming no firing probability decay with increasing slice depth (upper grey dashed line) or isometric firing probability decay (lower grey dashed line. **H)** Data from (D) and (H, best estimate) plotted to show the recruitment of feedback inhibition. **I)** Comparison of focal optogenetic stimulation to global (light fiber mediated) optogenetic stimulation. **Left,** Schematic illustration. **Middle,** Comparison of the AP probability of individual GCs at maximal stimulation power for focal and global stimulation assessed by cell attached recordings. **Right,** Comparison of the maximal IPSC amplitude under focal and global stimulation for individual GCs.

bioRxiv preprint doi: https://doi.org/10.1101/813188; this version posted October 21, 2019. The copyright holder for this preprint (which was not certified by peer review) is the author/funder, who has granted bioRxiv a license to display the preprint in perpetuity. It is made available under aCC-BY-NC 4.0 International license.

Spatial distribution of feedback inhibition

Recent evidence indicates that inhibition by individual PV^+ fast spiking hilar border interneurons is non-uniformly distributed over space, with decreasing connectivity and inhibition at greater distances from the interneuron [22,54]. To test whether feedback inhibition by the entire ensemble of feedback inhibitory interneurons also displays a spatial gradient we activated cell populations at 100 µm intervals along the GC layer while recording inhibition in individual GCs (**Fig. 3A**). Spatial profiles were recorded for increasing laser powers in cells in the superior as well as inferior blade of the DG (**Fig. 3B, C** respectively; n=8 cells for each blade). IPSC amplitudes across locations and powers were normalized to the maximal IPSC amplitude in each respective cell. This maximal amplitude did not differ between cells in different blades (366±40 vs 390±84 pA for superior and inferior blades respectively; t-test, P(df=14, t=0.258)=.0686). Next, we investigated the spatial organization of feedback inhibition at stimulation powers at which inhibition had saturated (**Fig. 3D, E**). In all GCs tested, the inhibition was greatest when stimulating in the direct vicinity of the recorded cell. Activating cells at increasing distances led to monotonically decreasing IPSC amplitudes for both blades. Importantly, the term distance here refers to the functional distance along the GC layer and not to Euclidean distance. However, inhibition was observed even at the most remote stimulation sites, indicating that even the most remote cells from the contralateral blade can contribute to the activation of feedback inhibition in a given GC. In order to statistically compare the relation of local versus remote inhibition between blades we defined a remote location in the contralateral blade at 800 µm from the recorded cell (measured along the GC layer and equidistant in all slices; **Fig. 3D, E**; grey lines) and compared it to the local IPSC (black lines). Remote inhibition was significantly smaller than local inhibition while no difference between blades or significant interaction was observed (**Fig. 3F**; two-way RM ANOVA; Distance: F(1,14)=3.341, P<.001; Blade: F(1,14)=2.615, P=.128; Interaction: F(1,14)=3.341, P=.089). Posttests suggested inhibition of inferior GCs by superior activation might be greater than vice versa. However, the difference was not significant (Sidak's

bioRxiv preprint doi: https://doi.org/10.1101/813188; this version posted October 21, 2019. The copyright holder for this preprint (which was not certified by peer review) is the author/funder, who has granted bioRxiv a license to display the preprint in perpetuity. It is made available under aCC-BY-NC 4.0 International license.

multiple comparison corrected posttest, P(df=28)=.932, P(df=28)=.051 for local and remote respectively).

Next, we investigated whether there are differences in the steepness of recruitment of local versus remote inhibition between blades (black and grey, respectively; **Fig. 3G, H**). To this end, we calculated the active cell fraction which produces half-maximal inhibition during local or remote stimulation for each individual slice. Comparison of the recruitment between the four groups revealed no differences between blades (**Fig. 3I,** two-way RM ANOVA; Distance: F(1,14)=7.889, P=.014; Blade: F(1,14)=0.5506, P=.470; Interaction: F(1,14)=0.0976, P=.759). However, local inhibition was significantly more steeply recruited than remote inhibition (1.99 ± 0.22% vs. 3.17 ± 0.57 % active cells for half-maximal inhibition).

Next, we tested if IPSCs elicited by increasing active GC populations differed between local and remote activation with respect to their kinetic properties. Since all previous data showed no indication of blade specific differences the analysis of the kinetics of feedback IPSCs were performed on the pooled data for both blades. Interestingly, local and remote inhibition differed in all tested respects (**Fig. 3J–M,** two-way RM ANOVAs with $df_{Distance}$=1,183, $df_{cell\ fraction}$=6,183 and $df_{interaction}$ =6,183). Local IPSCs occurred with shorter latency and lower jitter than remote IPSCs (**Fig. 3J, K;** Latency: P<.001, <.001 and =.031 for distance, cell fraction and interaction, respectively; Jitter: P<.001, =.037 and =.707 for distance, cell fraction and interaction, respectively). Furthermore, both latency and jitter decreased as larger populations were activated. IPSCs were also significantly slower in remote versus local inhibition. IPSC rise time was slightly shorter in the larger local IPSCs but did not correlate with the active cell fraction (**Fig. 3L**: P=.010, =.633 and =.388 for distance, cell fraction and interaction, respectively). Similarly, decay times were significantly shorter in local versus remote inhibition while they progressively increased with increasing stimulation power (**Fig. 3M**; P<.001, <.001 and =.124 for distance, cell fraction and interaction, respectively). These data demonstrate that remote inhibition shows greater delay, greater jitter and slower kinetics than local inhibition.

bioRxiv preprint doi: https://doi.org/10.1101/813188; this version posted October 21, 2019. The copyright holder for this preprint (which was not certified by peer review) is the author/funder, who has granted bioRxiv a license to display the preprint in perpetuity. It is made available under aCC-BY-NC 4.0 International license.

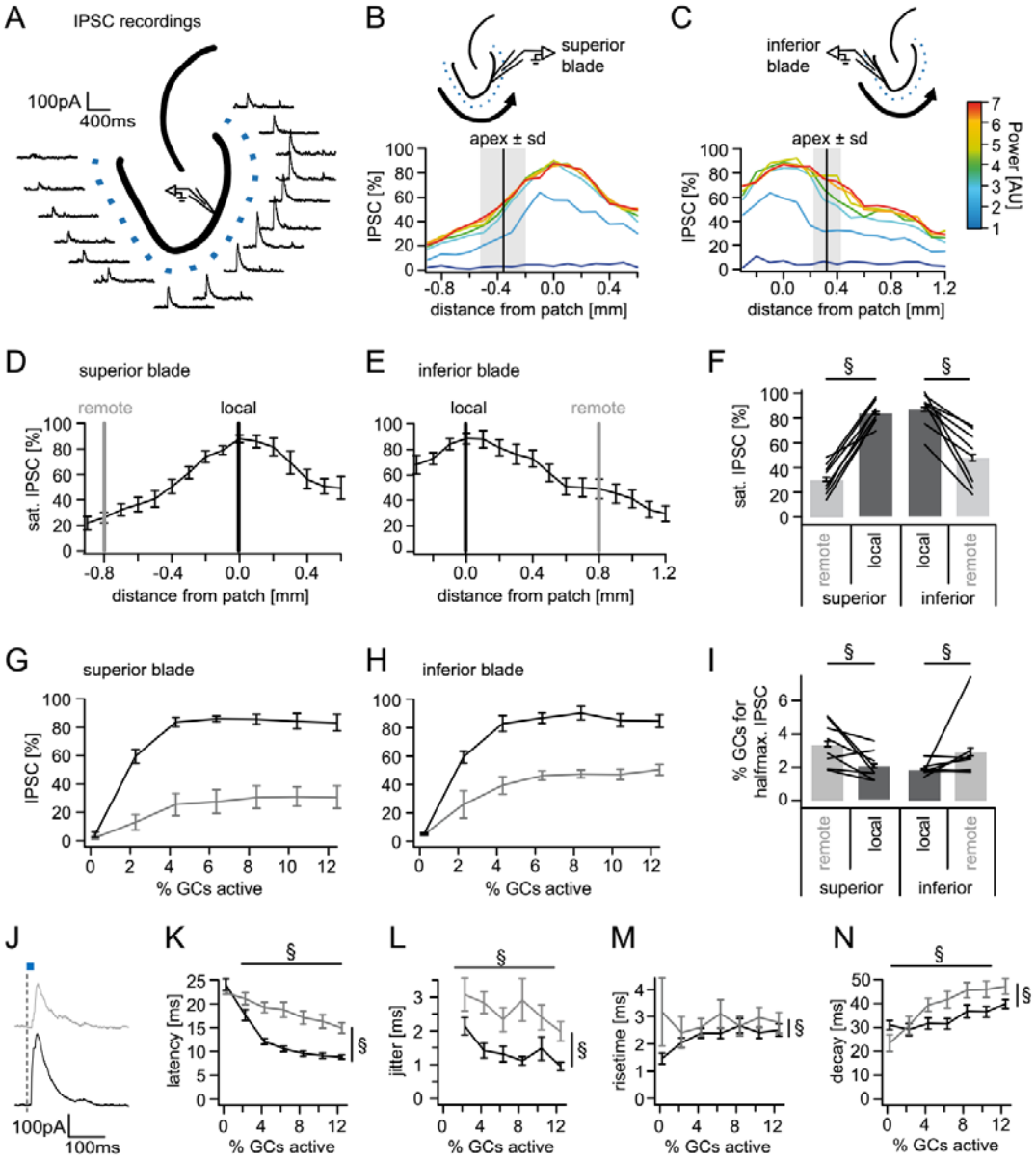

bioRxiv preprint doi: https://doi.org/10.1101/813188; this version posted October 21, 2019. The copyright holder for this preprint (which was not certified by peer review) is the author/funder, who has granted bioRxiv a license to display the preprint in perpetuity. It is made available under aCC-BY-NC 4.0 International license.

Fig. 3, Spatial organization of feedback inhibition. Feedback IPSCs recorded from an individual GC while GCs at varying distances were activated. **A)** Schematic illustration of the stimulation paradigm and example IPSC traces of an individual trial (P=3). **B, C)** Distribution of normalized IPSC amplitudes as a function of laser power and distance from stimulation spot for superior and inferior blade GCs (n=8 for each blade). The relative location of the DG apex ± standard deviation is indicated by the black bar and grey area respectively. **D, E)** IPSC distribution over space at saturation (P≥5). Black and grey bars indicate a local and a remote location at 800 µm from the recorded cell respectively. **F)** Comparison of the amplitude of the locally and remotely activated IPSCs at saturation (two-way RM ANOVA, overall test significance indicated by §) **G, H)** Comparison of the recruitment curves during local (black) or remote (grey) stimulation for superior and inferior blade respectively. **I)** Comparison of the cell fraction required for halfmaximal IPSC activation between stimulation sites and blades (two-way RM ANOVA overall test significance indicated by §). **J-M)** Temporal properties of IPSCs between local (black) and remote (grey) stimulation. To test for systematic variations of kinetic parameters with increasing active cell fractions as well as stimulation site two-way RM ANOVAs with no post tests were performed. Overall significance indicated by §. **K)** Latency from beginning of light pulse to IPSC **L)** temporal jitter of IPSCs (SD of latency within cells) **M)** 20% to 80% rise time **N)** IPSC decay time constant.

Short term dynamics in the feedback inhibitory microcircuit

Different connections within the feedback inhibitory microcircuit have been shown to variably facilitate or depress during trains of activity[21] (**Supplementary Table 1**). This makes it difficult to predict the net effect on the short term dynamics of GC feedback inhibition. We therefore characterized the frequency-dependence of net feedback inhibition using antidromic electrical stimulation as described above (**Fig. 4A-C**). In marked contrast to the CA1 region of the hippocampus [55], feedback IPSCs showed strong frequency dependent facilitation (**Fig. 4C**, n=10 cells, one-way RM ANOVA; Frequency: $F(2.69, 29.54)=13.99$, $P<.001$; Wilcoxon signed rank tests for deviation from unity at each frequency with Bonferroni corrected p-values; P=1, =.004, .002 and .002 for 1, 10, 30 and 50Hz, respectively). We found no evidence for a spatial gradient of net feedback inhibitory short term dynamics (**Supplementary Fig. 5**).

Because this unusual degree of facilitation may be important in allowing sparse activity of GCs to recruit significant inhibition over time, we further examined the underlying circuit mechanisms. Interestingly, previous literature on the DG feedback microcircuit almost exclusively reports short term depression of dentate interneuron inputs to GCs (**Supplementary Table 1**, blue rows), rendering our finding of pronounced facilitation at the circuit level even more striking. We therefore measured feedback excitation of hilar neurons

bioRxiv preprint doi: https://doi.org/10.1101/813188; this version posted October 21, 2019. The copyright holder for this preprint (which was not certified by peer review) is the author/funder, who has granted bioRxiv a license to display the preprint in perpetuity. It is made available under aCC-BY-NC 4.0 International license.

by stimulating mossy fiber axons as described above (**Fig. 4D-L**). Mossy cells and interneurons were classified according to their morpho-functional properties[31] (**Fig. 4D, E, G, H, J, K**). Cell classification was confirmed using unbiased k-means clustering (**Fig. 4K**). We found that feedback excitation of hilar cells displayed marked facilitation, which was similar for both INs and MCs (**Fig. 4F, I, L;** n=9, 12 respectively, two-way RM-ANOVA, Frequency: $F(3,57)=6.642$, $P<.001$; Cell type: $F(1,19)=0.0075$, $P=.932$; Interaction: $F(3,57)=0.743$, $P=.531$). Facilitation indices of hilar cells significantly deviated from one for all frequencies tested (**Fig. 4E, F**; n=23 cells; Wilcoxon signed rank tests with Bonferroni corrected p-values; $P<.001$ for all frequencies). These data demonstrate a pronounced frequency dependent net facilitation of the feedback inhibitory microcircuit, which is supported by strongly facilitating mossy fiber inputs to hilar cells.

bioRxiv preprint doi: https://doi.org/10.1101/813188; this version posted October 21, 2019. The copyright holder for this preprint (which was not certified by peer review) is the author/funder, who has granted bioRxiv a license to display the preprint in perpetuity. It is made available under aCC-BY-NC 4.0 International license.

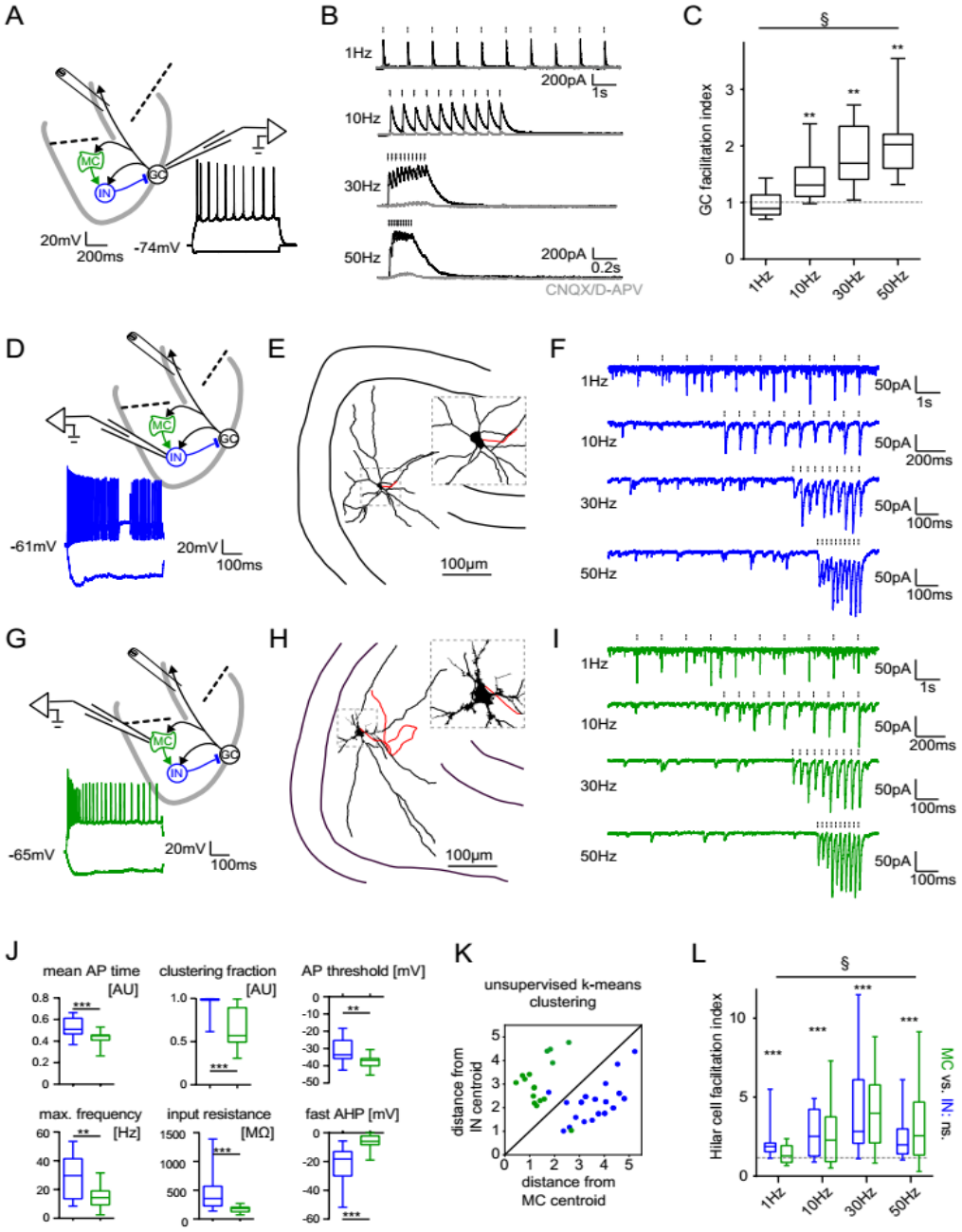

bioRxiv preprint doi: https://doi.org/10.1101/813188; this version posted October 21, 2019. The copyright holder for this preprint (which was not certified by peer review) is the author/funder, who has granted bioRxiv a license to display the preprint in perpetuity. It is made available under aCC-BY-NC 4.0 International license.

Fig. 4, Short term dynamics in the feedback inhibitory microcircuit. Trains of ten antidromic electrical stimulations at 1, 10, 30 or 50 Hz were applied to elicit disynaptic feedback inhibition or excitation of hilar cells (electrical stimulation artifacts were removed in all traces). **A, D, G)** Schematic illustration of the experimental setup and example traces of voltage responses to positive and negative current injections of GC and hilar cells (dashed lines indicate cuts to sever CA3 backprojections) **B)** Exemplary GC feedback IPSCs before (black) and after (grey) glutamatergic block (n = 7). **C)** Facilitation indices (mean of the last three IPSCs normalized to the first; n=10 cells) **D-L)** Hilar cells were manually classified into putative interneurons (blue) or mossy cells (green) based on their morpho-functional properties. **E)** Reconstruction of biocytin filled hilar interneuron (axon in red). **F)** Interneuron EPSCs in response to stimulation trains. **H)** Reconstruction of biocytin filled mossy cell (axon in red). **I)** Mossy cell EPSCs in response to stimulation trains. **J)** Quantification of intrinsic properties of hilar cells (see methods). **K)** k-means clustering based on intrinsic properties of hilar cells (coloring according to manual classification). **L)** Facilitation indices of classified hilar cells. (§ indicates significance in one-way RM ANOVA, * show significance in Bonferroni corrected Wilcoxon signed rank tests for deviation from 1).

Quantitative properties of the feedback circuit predict frequency dependent pattern separation

Together, these data indicate that the dentate feedback circuit is able to deliver strong, spatially graded inhibition with a high gain and the ability for temporal integration. To probe how these quantitative properties of the feedback circuit affect the pattern separation capability of the DG, we incorporated them into a biophysically realistic model of the lamellar microcircuit (**Fig. 5**) based on Santhakumar et al. (2005)[56,57], making use of their carefully experimentally constrained DG cell-types (**Fig. 5A, Supplementary Fig. 6A**). To maximize our models inferential value we clearly separated a tuning phase, in which we constrained the model by our experimental data, and an experimental phase, in which pattern separation was tested without further changes to the model. In the tuning phase, we first scaled up the model four-fold to contain 400 perforant path afferents (PPs), 2000 GCs, 24 basket cells (BCs), 24 hilar perforant path associated cells (HC) and 60 MCs (**Fig. 5A, B**). BCs, HCs and MCs comprise the feedback inhibitory circuit and BCs receive direct PP input thereby additionally mediating feedforward inhibition[32]. We then adapted the spatial extent of the target pools of BC and HC outputs to produce local and global inhibition respectively, reproducing the experimentally determined spatial tuning of *net* feedback inhibition (**Fig. 5C**). We further adjusted synaptic decay time constants and weights in order to reproduce the measured PSCs of hilar neurons and GCs and the empirical recruitment curves (**Fig. 5D, Supplementary Fig. 6**). Finally, we incorporated facilitation of the experimentally determined

bioRxiv preprint doi: https://doi.org/10.1101/813188; this version posted October 21, 2019. The copyright holder for this preprint (which was not certified by peer review) is the author/funder, who has granted bioRxiv a license to display the preprint in perpetuity. It is made available under aCC-BY-NC 4.0 International license.

magnitude into feedback excitatory mossy-fiber outputs, leading to GC IPSC facilitation in the experimentally observed range (**Fig. 5E, Supplementary Fig. 6B**). Together, these minimal adaptations resulted in a model with remarkably similar properties to our experimental findings (**Fig. C-E**). We therefore concluded the tuning phase of the model and proceeded to an in silico pattern separation experiment without further changes to the model.

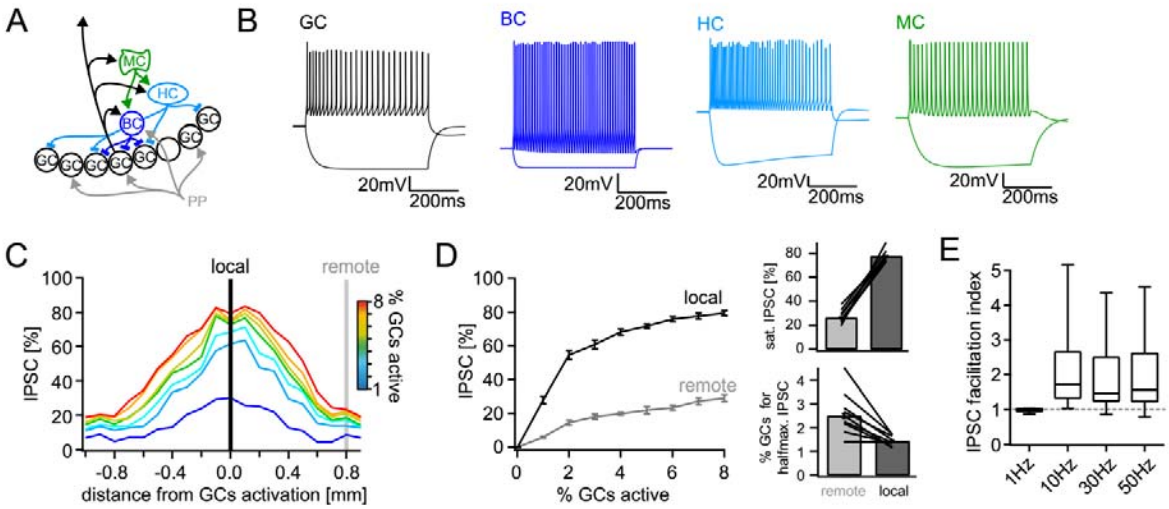

Fig. 5, Computational model of the DG feedback circuit. A biophysically realistic model of DG was tuned to capture the key quantitative features of the feedback circuit. All analyses were performed as for the real data (including IPSC normalization to maximal IPSC over space and power within each respective cell) **A)** Schematic of the model circuit. GC: granule cell, BC: basket cell, HC: hilar perforant path associated cell, MC; mossy cell. **B)** Intrinsic responses of model cell types to positive and negative current injections. **C)** Spatially graded net feedback inhibition following simulated focal GC activation. **D)** Local and remote recruitment curves of the feedback inhibitory circuit (left) and the resulting saturated IPSC amplitudes and GC fractions recruiting halfmaximal inhibition (right). **E)** Facilitation indices resulting from simulated, 10 pulse, frequency stimulation of GCs as above.

To investigate the implications for pattern separation we probed the ability of this model to separate PP input patterns with behaviorally relevant temporal structure and varying degrees of overlap [46,57]. Specifically, we created input trains with constant mean rate, but with either theta (10 Hz) or slow-gamma (30 Hz) modulation (**Supplementary Figs. 6C, 7A**), which are prominent during exploration and novelty exposure respectively [41,44]. To model rapid pattern separation in behaviorally relevant timescale we chose an input duration of approximately five theta cycles (600ms, corresponding to the approximate duration of place cell spiking during traversal of its place field). To obtain a range of input similarities, we generated input

bioRxiv preprint doi: https://doi.org/10.1101/813188; this version posted October 21, 2019. The copyright holder for this preprint (which was not certified by peer review) is the author/funder, who has granted bioRxiv a license to display the preprint in perpetuity. It is made available under aCC-BY-NC 4.0 International license.

patterns in which 24 of 400 PP afferents were activated (**Fig. 6A, Supplementary Fig. 6**) and compared pairs of such patterns ranging from no overlap (two separate sets of afferents) to complete overlap (identical trains in the same 24 afferents in both patterns). Each model network was run with 25 input patterns leading to a total of 325 comparisons (data points in **Fig. 6C**). To quantify pattern separation we compared input correlation (R_{in}) to output correlation (R_{out} ; **Fig. 6B**) both measured as Pearson's R between the population rate vectors over the full 600ms time window [9,12]. Our full, tuned model reliably decreased the population vector correlations for similar patterns ($0<R_{in}<1$) thereby demonstrating robust pattern separation over the whole range of input similarities ($R_{out}<R_{in}$; **Fig. 6C**, left). Next, we isolated the contribution of feedback inhibition to pattern separation by rerunning the same input pattern combinations on the network in which mossy fiber outputs to interneurons were removed (**Fig. 6C,** middle). This eliminated HC activity and reduced BC spiking by nearly 50% (not shown). Note that removing mossy fiber outputs also eliminates BC activity through cooperative activation by summating feedforward and feedback inputs[32]. Removal of all inhibitory outputs led to a further decrease in pattern separation, demonstrating the effect of additionally removing feedforward inhibition (**Fig. 6C**, right). As expected these manipulations increased both the fraction of active GCs and the activity per GC (**Supplementary Fig. 7B, C**). In order to quantify the respective pattern separation effects over the full range of input similarity, we computed the bin wise mean R_{out} (Fig. 6C, R_{in} bin-width: 0.1, dashed line) and measured the area to the identity line (**Fig. 6C**, black lines). The resulting mean ΔR_{out} was calculated for seven separate random networks, each challenged with theta as well as slow-gamma modulated inputs in each of the three conditions. Both the frequency of the input modulation as well as network manipulatons significantly affected pattern separation (**Fig. 6D**; two-way RM ANOVA with both factors matching, condition: $F(2,12)=145.1$, $P<.001$; frequency: $F(1,6)=31.48$, $P=.001$; interaction: $F(2,12)=11.77$, $P=.002$; n=7 random network seeds for these and all subsequent analyses). Specifically, both feedback and feedforward inhibition significantly contributed to pattern separation (Sidak's multiple comparison posttest, $P(df=12, t=11.33)<.001$ and $P(df=12, t=5.36)<.001$, respectively).

bioRxiv preprint doi: https://doi.org/10.1101/813188; this version posted October 21, 2019. The copyright holder for this preprint (which was not certified by peer review) is the author/funder, who has granted bioRxiv a license to display the preprint in perpetuity. It is made available under aCC-BY-NC 4.0 International license.

To quantify the isolated effects of feedback and feedforward inhibition we computed the difference in R_{out} between the respective conditions for each individual comparison (i.e. data point in Fig. 6C). For instance, the individual comparison shown in Fig. 6A, will lead to a single R_{out} value in the network with MF inputs to interneurons (full model), which is subtracted from the corresponding R_{out} value in the same network without this input (no FB). This procedure isolates the effect of interest (ΔR_{out}) for each individual comparison, controlling for other sources of variability. A single pattern separation measure was then obtained as before, as the area under the curve of bin-wise means of these ΔR_{out} values (**Fig. 6E**, inset). We found a significant effect of both inhibitory motif and frequency domain (**Fig. 6E**; two-way RM ANOVA with both factors matching, Motif: F(1,6)=15.58, P=.008; Frequency: F(1,6)=9.91, P=.020; Interaction: F(1,6)=76.37, P<.001). Posttests revealed that the frequency dependence of pattern separation was driven by feedback inhibition (Sidak's multiple comparison posttest: FB: P(df=6, t=13.68)<.001; FF: P(df=6, t=1.33)=.412. Interestingly, this frequency dependence of feedback inhibition mediated pattern separation was particularly pronounced for highly similar input patterns ($0.9<R_{in}<1$; Fig. 6E, right; Motif: F(1,6)=261.7, P<.001; Frequency: F(1,6)=108.1, P<.001; Interaction: F(1,6)=109.5, P<.001; Sidak's multiple comparison posttest: FB: P(df=6, t=15.78)<.001; FF: P(df=6, t=0.98)=.595). It has recently been emphasized, that the assessment of pattern separation can depend critically on the pattern similarity measure used[8,58]. Therefore we tested the robustness of this result for two alternative similarity measures, namely normalized dot product (NDP, also known as cosine similarity) and pattern overlap (# of coactive/ # of totally active cells; **Supplementary Fig. 7).** The frequency dependence of feedback inhibition mediated pattern separation, especially for highly similar inputs, proved robust for all three similarity measures (see figure legend for statistics).

Effect of spatial tuning and facilitation of net feedback inhibition

Next we investigated the specific effects of two interesting empirical findings of the present study, 1) the spatial tuning and 2) the facilitation of the feedback circuit (**Supplementary Fig. 8)**. To this end we undertook two targeted, minimal manipulations of the full tuned network.

bioRxiv preprint doi: https://doi.org/10.1101/813188; this version posted October 21, 2019. The copyright holder for this preprint (which was not certified by peer review) is the author/funder, who has granted bioRxiv a license to display the preprint in perpetuity. It is made available under aCC-BY-NC 4.0 International license.

To probe the effect of spatially graded inhibition, we redistributed BC output synapses to a global target pool (the whole GC population), leading to spatially uniform inhibition (global FB; **Supplementary Fig. 8B; 8E, left**). To probe the effect of facilitation, we removed facilitation from mossy fiber outputs (**Supplementary Fig. 8C; E, right**). We isolated the effects of these manipulations by pairwise comparison to the corresponding full tuned networks as described above (**Supplementary Fig. 8F-I**). The results showed a small but significant contribution of facilitation (~20% of the isolated FB effect for both frequency paradigms), but not spatial tuning to pattern separation (**Supplementary Fig. 8G, left**; Wilcoxon signed rank test for deviation from 0, n=7, Bonferroni corrected P-values: P=.031 and P=1 respectively for 10Hz; P=.031 and P=1 respectively for 30Hz). We noted that while spatial tuning did not affect mean pattern separation, it appeared to reduce its variability (CoV) for a given input similarity (**Supplementary Fig. 8G, right**; Wilcoxon signed rank test for deviation from 0, n=7, Bonferroni corrected P-values: P=.031 and P=.750 for tuning and facilitation respectively at 10Hz; P=0.438 and P=1 respectively at 30Hz).

bioRxiv preprint doi: https://doi.org/10.1101/813188; this version posted October 21, 2019. The copyright holder for this preprint (which was not certified by peer review) is the author/funder, who has granted bioRxiv a license to display the preprint in perpetuity. It is made available under aCC-BY-NC 4.0 International license.

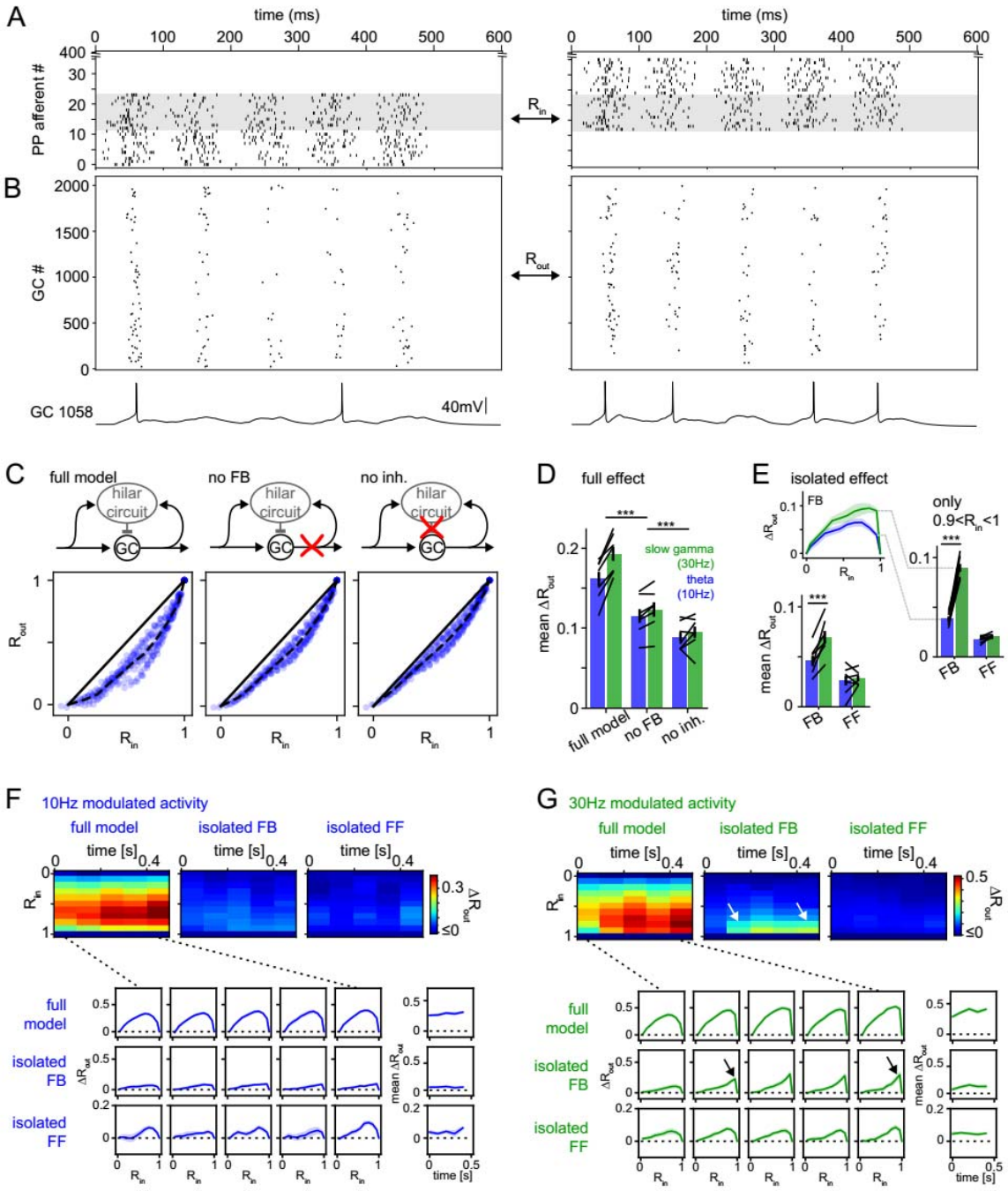

bioRxiv preprint doi: https://doi.org/10.1101/813188; this version posted October 21, 2019. The copyright holder for this preprint (which was not certified by peer review) is the author/funder, who has granted bioRxiv a license to display the preprint in perpetuity. It is made available under aCC-BY-NC 4.0 International license.

Fig. 6, Frequency dependent pattern separation of temporally structured inputs. The quantitative DG model was challenged with theta (10Hz) or slow gamma (30Hz) modulated input patterns with defined overlap to probe its pattern separation ability. **A)** Pair of theta modulated perforant path input patterns in which 50% of afferents overlap (grey area). **B)** Resulting pair of GC output patterns of the full tuned network. **Bottom:** Representative individual GC underlying the observed patterns. **C)** Comparison of 325 input pattern pairs and their resulting output pattern pairs. Each pair is characterized by its rate vector correlation for inputs (R_{in}) and outputs (R_{out}), where rates are measured over the full 600 ms time window. Dashed black lines represent the bin-wise mean R_{out} (in R_{in} bins of 0.1). **Left:** full tuned model, **middle:** model without mossy fiber inputs to interneurons, **right:** model without inhibitory synapses. **D)** Full pattern separation effects (mean ΔR_{out}) of all three conditions for both frequency domains quantified as the area enclosed by the dashed and unity lines in (C). Black lines represent individual network seeds. Two-way RM ANOVA indicated significance of condition, frequency and interaction, * indicate significance in Sidak's posttests between individual conditions. **E)** Isolated effects of feedback and feedforward motifs obtained by pairwise subtraction of R_{out} between conditions for each individual comparison. The inset shows the resulting ΔR_{out} for each R_{in} bin. The area under the curve quantifies the mean ΔR_{out} as in (D). Two-way RM ANOVA indicated significance of condition, frequency and interaction. *** indicate p<0.001 in Sidak's posttest. **F)**. 100ms time-resolved pattern separation effects of the full model, isolated FB or FF inhibition for theta modulated input (10Hz). All analyses were performed as above but with rate vector correlations computed for 100 ms time windows. The bottom insets show ΔR_{out} as a function of input similarity for each time window. The bottom right insets show the evolution of the mean ΔR_{out} over time. **G)** Same as (F) but for slow gamma (30Hz) modulated inputs. Arrow indicate the region of selectively increased pattern separation. Data in D-G represent mean ± SEM of n=7 random network seeds.

Frequency dependent pattern separation is robust over analysis scales

So far, all pattern separation analyses were conducted on the population rate vectors during a 600 ms time window. However, many neural computations are likely to occur on shorter timescales, such as within individual theta cycles (~100 ms)[19,59]. Indeed, the time window in which correlation is recorded can nontrivially affect the resulting correlation, depending on the timing of spikes within it[58]. We therefore computed the networks pattern separation ability within 100 ms time windows, revealing i) the pattern separation ability within such short timescales and ii) the temporal evolution of pattern separation throughout a 600 ms stimulus presentation (**Fig. 6F, G**). We find that pattern separation occurs even within a single theta cycle, including a contribution of feedback inhibition in both frequency paradigms (mean ΔR_{out} significantly different from 0 within the first 100 ms bin, Wilcoxon signed rank test with Bonferroni corrected p-values: P=.031, =.031 for full and FB effect respectively in both paradigms). While mean ΔR_{out} did not differ between frequency paradigms within this first time window, it was significantly elevated in the 30 Hz paradigm in all subsequent time windows (full model effect, two-way RM ANOVA, P<.001, <.001 and =.004 for time-bin,

bioRxiv preprint doi: https://doi.org/10.1101/813188; this version posted October 21, 2019. The copyright holder for this preprint (which was not certified by peer review) is the author/funder, who has granted bioRxiv a license to display the preprint in perpetuity. It is made available under aCC-BY-NC 4.0 International license.

frequency and interaction respectively, Sidak's posttest P=.234 for 1st bin and P<.001 for all subsequent bins). Again, the selective increase during slow-gamma modulated inputs was driven by feedback inhibition (isolated FB effect, two-way RM ANOVA, P=.007, <.001 and =.041 for time-bin, frequency and interaction respectively, Sidak's posttest P=.708 for 1st bin and P<.002 for all subsequent bins), including a contribution from MF facilitation (**Supplementary Fig. 8**). As above, the effect was predominantly driven by the separation of highly similar input patterns (isolated FB effect, R_{in}>0.5; two-way RM ANOVA on last time-bin, P<.001, =.010 and <.001 for R_{in}-bin, frequency and interaction respectively, Sidak's posttest on differences between frequency paradigms for each input similarity: P=1 for R_{in}<0.6 and P=.032 to P<.001 for R_{in}= 0.6 to 0.9). These results were robust when analysis time windows were decreased even further (33 ms, **Supplementary Fig. 9**). This 33 ms resolved analysis additionally reveals that the pattern separation effect, particularly of feedback inhibition, ramps up within a 100 ms window, becoming effective only at the end of a theta cycle (**Supplementary Fig. 9B**).

Next we asked if the frequency dependence of feedback inhibitory pattern separation was sensitive to variations of the inhibitory decay time constants and if there might be an interaction between these decay time constants and the frequency range at which pattern separation is most effective (**Supplementary Fig. 10**). Remarkably, we found the differential effect between 10 & 30 Hz to be highly robust across a range of different decay time-constants (0.5x to 5x the experimentally matched decay, **Supplementary Fig. 10A-C, Table 2**). Furthermore, the selective enhancement of feedback inhibitory pattern separation of highly similar inputs was robust over the entire gamma range (up to 100Hz, **Supplementary Fig. 10D, E**).

Finally, we tested if our main results were robust to alterations in the relative strengths of feedforward vs. feedback inhibition. Since, our model is closely constrained with respect to the recruitment and functional properties of the feedback circuit, we are confident about the resulting computational inferences concerning this circuit. However, the model does not allow

bioRxiv preprint doi: https://doi.org/10.1101/813188; this version posted October 21, 2019. The copyright holder for this preprint (which was not certified by peer review) is the author/funder, who has granted bioRxiv a license to display the preprint in perpetuity. It is made available under aCC-BY-NC 4.0 International license.

strong inferences about the relative roles of feedback and feedforward inhibition, and it is thus necessary to probe if extremely powerful feedforward inhibition might occlude the effects described here. We therefore selectively enhanced the feedforward inhibitory circuit in our model by increasing the PP to BC circuit 2x (**Supplementary Fig. 11**). This robustly increased the feedforward inhibitory contribution to pattern separation above that of feedback inhibition (**Supplementary Fig. 11B**). However, it did not affect the frequency dependence of the feedback inhibitory effect. Indeed, for highly similar input patterns, the feedback inhibitory effect was so prominently enhanced during gamma input, as to again dominate the feedforward inhibitory effect (**Supplementary Fig. 11C**).

Together these results suggest that frequency dependence is a key feature of the feedback inhibitory microcircuits and predict that feedback inhibition selectively boosts the separation of highly similar input patterns during gamma oscillations.

bioRxiv preprint doi: https://doi.org/10.1101/813188; this version posted October 21, 2019. The copyright holder for this preprint (which was not certified by peer review) is the author/funder, who has granted bioRxiv a license to display the preprint in perpetuity. It is made available under aCC-BY-NC 4.0 International license.

Discussion

Across brain regions and species, inhibitory circuits contribute critically to regulating the sparsity and overlap of neural representations [1,10,11,20]. In most, if not all brain regions, feedback inhibition is viewed as important in these capabilities, by directly mediating competition between active cell ensembles [46,60,61]. In the mammalian DG, feedback inhibition is implemented by an intricate network of interneurons that is capable of delivering spatiotemporally defined inhibition to the principal cell population. How *net* feedback inhibition is functionally organized in mammals, and how it may contribute to pattern separation of biologically relevant, temporally structured input patterns is, however, poorly understood.

Quantitative physiological properties of DG feedback inhibition

We have therefore quantitatively described the recruitment of *net* feedback inhibition by defined GC population sizes in space and time in the hippocampal DG, a structure in which sparse activity and inhibition are thought to critically contribute to the function of pattern separation [14–16,20,62]. The proposed role of the feedback inhibitory circuit depends critically on its dynamic range, i.e. the relation between the number of active principal cells and the resulting feedback inhibition. This property of the feedback circuit is determined by complex, mainly hilar cellular connectivity patterns [21,22] (**Supplementary Table 1**). While delving into detailed cell-cell connectivities is clearly important, such studies do not allow the quantitative determination of the gain and dynamic range of *net* feedback inhibition [50,52]. Using two complementary experimental approaches, we found that *net* feedback inhibition is steeply recruited by sparse populations of GCs (<4%). Accordingly, the gain and sensitivity of the circuit are well suited to strongly modulate feedback inhibition within the range of GC activity reported in vivo[42,63]. Additionally, we have described in detail the temporal and spatial distribution of inhibition delivered by feedback circuits in the DG.

bioRxiv preprint doi: https://doi.org/10.1101/813188; this version posted October 21, 2019. The copyright holder for this preprint (which was not certified by peer review) is the author/funder, who has granted bioRxiv a license to display the preprint in perpetuity. It is made available under aCC-BY-NC 4.0 International license.

Frequency-dependent effects of feedback inhibition on pattern separation

How do the properties of feedback circuits influence the pattern separation capability of the dentate gyrus? To address this question we adapted an established biophysically realistic computational model of the DG circuitry [56,57]. We first carefully constrained the model to match the spatial and temporal properties of *net* feedback inhibition as assessed in our physiological data. We then fixed all model parameters, and proceeded to probe the ability of this circuit to perform pattern separation on temporally complex oscillatory inputs. The major, highly robust, result of this computational study was that the impact of feedback inhibition on pattern separation is frequency-dependent. Specifically, we find that the separation of input patterns during gamma oscillations >30 Hz is powerfully and selectively enhanced by the feedback circuit. Remarkably, this mechanism was particularly efficient for very similar input patterns. Such an effect has not been discovered in earlier modeling studies, because most models have discretized time, calculating the pre-inhibition population activity, the resulting inhibition, and the inhibition-corrected population activity in a single time step, sometimes assuming an average corrected population rate within this time step [46,64,65]. Thus, they do not capture temporal features of feedback circuits. On the other hand, a number of spike based, temporally resolved models have considered only temporally unstructured (Poisson) inputs [57,66–68]. We suggest that the precise spatiotemporal organization of the feedback circuit, together with the temporal structure of DG inputs is a crucial determinant of pattern separation. Indeed, the DG and its inputs have a strong, behaviorally relevant, temporal structure [42,69,70]. Novelty experience can induce increased gamma and beta range activity [41,71,72], and explorative activity with rearing is also associated with increased gamma oscillations [73]. A recent model has addressed how fast, rhythmic gamma-frequency feedback inhibition may implement a type of 'k-winners-take-all' operation, a basic computational component of pattern separation models[60], though this model relies on faster synaptic timescales than we observed in our compound IPSCs. Perhaps most interestingly, the occurrence of oscillations in the slow-gamma range has recently been reported to be causally related to associative memory formation [41,44], a process thought to require pattern

bioRxiv preprint doi: https://doi.org/10.1101/813188; this version posted October 21, 2019. The copyright holder for this preprint (which was not certified by peer review) is the author/funder, who has granted bioRxiv a license to display the preprint in perpetuity. It is made available under aCC-BY-NC 4.0 International license.

separation. Consistent with this finding, Hsiao et al. [43] report DG driven gamma entrainment of CA3, the presumed primary storage location of associative memories. Together, this suggests that the dentate pattern separator may be optimized to rapidly detect subtle degrees of difference within the environment in gamma-dominated exploratory brain states, a capability likely to support successful memory encoding of novel environmental features, and potentially aiding in rapid discrimination during recall.

Importantly, the frequency-dependent pattern separation was driven by the feedback circuit, and was highly robust to various alterations to the model. For instance, increasing the level of feedforward inhibition enhanced its contribution to pattern separation, but did not affect feedback inhibitory frequency-dependence. This effect was also robust when varying the decay time constants of the inhibitory synaptic conductances, the time windows of analysis, or the similarity measure employed. Together this suggests that frequency-dependent pattern separation is a key property of the local inhibitory feedback circuit. Importantly, this does not preclude that additional, long range projections may add further complexity[74]. Also note that in addition to the instantaneous pattern separation mechanisms investigated here, potentially complementary mechanisms at much longer time scales have been proposed involving ongoing neurogenesis [75–80].

Spatiotemporal organization of inhibition and pattern separation

The model also allowed us to examine the impact of the spatiotemporal organization of inhibition on pattern separation. Facilitation of feedback circuits produced a small but robust enhancement of pattern separation, while spatial tuning of feedback inhibition did not. The facilitation of feedback inhibition is a remarkable feature of the DG, which we to our knowledge have described for the first time. It is in marked contrast to area CA1, where somatically measured feedback inhibition shows strong depression [55,81] and is particularly surprising given the prevalence of depression in the literature on pairwise connections (**Supplementary Table 1**). Our physiological and modeling data suggest that the strong facilitation of the mossy fiber input to the feedback circuit is the principal mediator of this net

bioRxiv preprint doi: https://doi.org/10.1101/813188; this version posted October 21, 2019. The copyright holder for this preprint (which was not certified by peer review) is the author/funder, who has granted bioRxiv a license to display the preprint in perpetuity. It is made available under aCC-BY-NC 4.0 International license.

facilitation. The effect of facilitation on pattern separation is intuitive, since this allows the feedback circuit to integrate GC activity over time, and convert it to inhibition.

In our model, spatial tuning of feedback inhibition had no effects on pattern separation. This may derive from the fact that PP inputs were spatially broad and random[82,83]. In general, the effect of localized inhibition could be more relevant if synchronously activated populations of GCs are locally clustered [84]. For instance, GCs in the inferior and superior blades of the DG are known to be differentially active [85,86]. Accordingly, localized inhibition might be important for independent processing between the two blades. An alternative function of spatially graded inhibition has been proposed by [54], who suggest that it is more effective in promoting synchronous gamma oscillations. Accordingly, spatial tuning may play a role in creating the oscillatory dynamics, found here to critically impact the feedback inhibitory pattern separation performance.

Together, this study provides the first comprehensive, quantitative description of the spatiotemporal properties of the DG feedback inhibitory microcircuit, and predicts that these properties will selectively enhance the separation of highly similar input patterns during learning- related gamma oscillations. This mechanism may be relevant for understanding disease states in which there is a coincidence of dentate gyrus-centered pathology with abnormal oscillatory activity, and memory and pattern separation deficits (i.e. temporal lobe epilepsy, Alzheimer's disease, schizophrenia)[14,87–89].

bioRxiv preprint doi: https://doi.org/10.1101/813188; this version posted October 21, 2019. The copyright holder for this preprint (which was not certified by peer review) is the author/funder, who has granted bioRxiv a license to display the preprint in perpetuity. It is made available under aCC-BY-NC 4.0 International license.

Materials and Methods

Animals and Slice Preparation: All animals were treated according to the University of Bonn Animal Experiment Guideline, minimizing unnecessary pain and discomfort. Experiments were performed on horizontal hippocampal slices of 21 to 97 day old mice. Ca^{2+} imaging and a subset of dual recording experiments were performed in C57/Bl6 mice obtained from Charles River Laboratories (Wilmington, Massachusetts, USA). Optogenetic experiments and the remaining dual recording experiments were performed on double transgenic offspring of Tg(Prox1-cre)SJ39Gsat/Mmucd) obtained from MMRRC UC Davis as cryopreserved sperm and rederived in the local facility [90,91] and Ai32-mice (B6;129S-Gt(ROSA)26Sor$^{tm32(CAG-COP4*H134R/EYFP)Hze}$/J, Jackson Laboratory, Bar Harbor, USA). For preparation the animals were deeply anesthetized with Isoflurane (Abbott Laboratories, Abbot Park, USA) and decapitated. The head was instantaneously submerged in ice-cold carbogen saturated artificial cerebrospinal fluid (containing in mM: NaCl, 60; sucrose, 100; KCl, 2.5; NaH_2PO_4, 1.25; $NaHCO_3$, 26; $CaCl_2$, 1; $MgCl_2$, 5; glucose, 20) and the brain removed.

Horizontal 350 µm thick sections were cut with a vibratome (VT1200 S, Leica, Wetzlar, Germany, 300 µm sections for hilar recordings). To obtain maximum-connectivity-plane slices the brain was glued to its dorsal surface (compare Bischofberger et al., 2006). The slicing depth at which the temporal pole of the hippocampus first became visible was noted (depth = 0 µm). From here the first four sections were discarded (up to a depth of 1400 µm). The following two to three sections were secured such that one further section before the beginning of the dorsal hippocampus (approximately 2400 µm) could be discarded. Slices were incubated at 35 °C for 20 to 40 minutes and then stored in normal ACSF (containing in mM: NaCl, 125; KCl, 3.5; NaH_2PO_4, 1.25; $NaHCO_3$, 26; $CaCl_2$, 2.0; $MgCl_2$, 2.0; glucose, 15) at room temperature. Recordings were performed in a submerged recording chamber at 33-35 °C under constant superfusion with carbogen saturated ACSF (3 ml/min). Experiments were performed in the superior blade unless otherwise indicated.

bioRxiv preprint doi: https://doi.org/10.1101/813188; this version posted October 21, 2019. The copyright holder for this preprint (which was not certified by peer review) is the author/funder, who has granted bioRxiv a license to display the preprint in perpetuity. It is made available under aCC-BY-NC 4.0 International license.

Electrophysiological Recordings: Hippocampal dentate GCs were visually identified using infrared oblique illumination contrast microscopy in a 20x or 60x water immersion objective (Olympus, XLumPlanFl, NA0.95W or Nikon, N60X-NIR Apo, NA1.0W) on an upright microscope (TriMScope®, LaVision Biotech, Bielefeld, Germany or Nikon Eclipse FN1, Tokyo, Japan). For IPSC measurements the whole-cell patch-clamp configuration was established with a low chloride cesium-methane-sulfonate based intracellular solution (intracellular solution containing in mM: CH_3O_3SCs, 140; 4-(2-hydroxyethyl)-1-piperazineethanesulfonic acid (HEPES-acid), 5; ethylene glycol tetraacetic acid (EGTA), 0.16; $MgCl_2$, 0.5; sodium phosphocreatine, 5; glucose, 10). For GC current clamp experiments a low chloride solution (CC-intracellular solution containing in mM: K-gluconate, 140; 4-(2-hydroxyethyl)-1-piperazineethanesulfonic acid (HEPES-acid), 5; ethylene glycol tetraacetic acid (EGTA), 0.16; $MgCl_2$, 0.5; sodium phosphocreatine, 5) was used. GCs with input resistances greater than 300 MΩ were discarded in order to exclude immature GCs [92]. Hilar cells were recorded with intracellular solution containing in mM: K-gluconate, 140; KCL, 5; HEPES-acid, 10; EGTA, 0.16; Mg-ATP, 2; Na_2-ATP, 2; pH adjusted to 7.25; 277mmol/kg without biocytin. 0.3% biocytin (Sigma-Aldrich, B4261). In all imaging experiments and a subset of optogenetic experiments the intracellular solution additionally contained 100 µM Alexa 594 hydrazide sodium salt (Life Technologies, Carlsbad, USA). The identity of visually and electrophysiologically identified mature GC was confirmed by their dendritic morphology after dye filling in every case tested. Pipette resistance of the patch pipettes was 3 – 7 MΩ. Voltage-clamp recordings were performed with a Multiclamp 700B (Molecular Devices, Sunnyvale, USA) or a BVC-700A amplifier (Dagan Corporation, Minneapolis, USA). Current-clamp recordings were performed with a Multiclamp 700B. Voltage or current signals were digitized with a Digidata 1322A (Molecular Devices) or (Instrutech ITC-16, Heka Electronics, Ludwigshafen, Germany) at 10 or 50 kHz and recorded using Clampex 10.2 (Molecular Devices) or Igor Pro 6 (Wavemetrics, Lake Oswego, USA) on a PC running Windows XP. For IPSC measurements cells were held at 0 mV including liquid-junction potential correction (estimated at 16 mV). To aid the voltage clamp throughout the cell, this depolarized

bioRxiv preprint doi: https://doi.org/10.1101/813188; this version posted October 21, 2019. The copyright holder for this preprint (which was not certified by peer review) is the author/funder, who has granted bioRxiv a license to display the preprint in perpetuity. It is made available under aCC-BY-NC 4.0 International license.

membrane potential was slowly approached during a 15min pre-equilibration period, during which Cs^+ entered the cell. For CC-recordings liquid junction potential was not corrected. IPSCs were normalized to the maximally elicited IPSC over space and power for each respective cell. Importantly, this normalization does not require prespecification of the location or power at which a respective cell's maximum occurs. Note, that due to this procedure all normalized IPSC values are by definition below 100%. Chemicals for electrophysiological experiments were obtained from Sigma-Aldrich (St. Louis, USA). All drugs were purchased from Tocris Bioscience (Bristol, UK).

Dual Patch Experiments: Two GCs within 100 µm of each other were recorded. To test for single GC induced feedback inhibition 10 to 15 trains of 10 APs at 100 Hz were elicited by brief (3 ms) current injections in one cell. Inhibition was monitored either in VC, while holding the cell at 0 mV to allow the detection of small IPSCs (**Supplementary Fig. 2**, n=7 cell pairs, 7 directions) or current clamp while holding the cell at -60 mV, allowing to probe for inhibition in both directions (not shown, n=4 cell pairs, 8 directions).

Ca^{2+} Imaging: Dye loading was modified from [93] and performed in the submerged chamber at 35°C under constant superfusion. Briefly, a dye solution containing: 1 mM Oregon Green® 488 BAPTA-1 acetoxy-methyl ester (OGB-1 AM); 2% pluronic F-127;150mM; 2.5mM KCl; 10mM HEPES). The dye was injected into the slice along the superior blade of the GC layer using standard patch pipettes (4-5 locations, 100 µm intervals, 30µm depth, 3 minutes at 500 mbar per location). Recordings were started at least 45 minutes after the staining procedure. Population Ca^{2+} Imaging was performed using a multibeam two-photon fluorescence microscope (TriMScope®, LaVision Biotech, Bielefeld, Germany) with excitation light at 810 nm. Images were acquired with a digital CMOS camera (ORCA-Flash, Hamamatsu) through a high numerical aperture 20x water immersion Objective (XLumPlanFl, NA-0.95, Olympus). This allowed imaging of a large field of view (320 x 240 µm) with high spatial and temporal resolution (1920 x 1440 pixels, 20 Hz) at acceptable signal to noise ratios. Time series were processed with ImageJ 1.48o and IGOR Pro 6.3 in a semiautomatic manner. Regions of

bioRxiv preprint doi: https://doi.org/10.1101/813188; this version posted October 21, 2019. The copyright holder for this preprint (which was not certified by peer review) is the author/funder, who has granted bioRxiv a license to display the preprint in perpetuity. It is made available under aCC-BY-NC 4.0 International license.

interest were manually placed onto all well loaded cells which remained visible throughout the experiment. Ca^{2+} fluorescence increase normalized to baseline (ΔF/F) traces of individual cells were calculated without background subtraction. The fraction of responders for each time series was extracted by automatic thresholding at ΔF/F = 0.94%. The threshold was determined by combined cell-attached and Ca^{2+} imaging experiments. Note, that for these experiments the stimulation electrode was placed into the hilus in order to obtain a sufficient number of true positive responders. The imaged cell population comprised on average 46 ± 18 (standard deviation) cells (n = 23 slices). The active cell fraction corresponds to the fraction of responders normalized to the dye loaded population within each section. To assess the spatial distribution of cell activation in imaging experiments, ΔF/F projections were created by averaging and smoothing four frames during the transient and four frames at baseline fluorescence and then calculating the pixel wise ΔF/F.

Antidromic electrical stimulation was achieved using a bipolar cluster microelectrode (FHC, Bowdoin, USA) connected to a digital stimulus isolator (AM-systems, Sequim, USA), placed into stratum lucidum in the CA3 region. IPSCs at individual powers were elicited 5 to 13 times at 0.1 Hz and averaged (0.1 ms pulse time). The amplitude beyond which the stimulus isolator could not pass the full current, determined the maximal stimulation amplitude for each experiment.

In order to obtain the input-output relationships of the feedback inhibitory circuit data, each variable was averaged over slices by power. This was necessary since only a small subset of experiments in which inhibition was completely blocked could also be successfully imaged (6 of 8 sections). Due to the small numbers of active cells throughout the entire dataset with sufficient dye loading (n = 23 slices) analysis of only these 6 slices leads to a very piecemeal recruitment curve. A more accurate estimation of the recruitment of feedback inhibition was obtained by averaging the cell activation and inhibition over all respectively appropriate slices and relating them by power. Note that while the fraction of activated cells in non-MCP

bioRxiv preprint doi: https://doi.org/10.1101/813188; this version posted October 21, 2019. The copyright holder for this preprint (which was not certified by peer review) is the author/funder, who has granted bioRxiv a license to display the preprint in perpetuity. It is made available under aCC-BY-NC 4.0 International license.

sections (not included in the quantitative analysis) was mostly zero, IPSCs were almost always present (in 28 of 29 cells in non-MCP sections).

Optogenetic Stimulation: Focal optogenetic stimulation was achieved through a galvanometer driven spot illumination device coupled to a 473 nm DPSS Laser (UGA-40, DL-473, Rapp Optoelectronics, Hamburg, Germany) on an upright microscope (Nikon Eclipse FN1, Tokyo, Japan). The width of the resulting stimulation spot at the focal plane was 8.36 ± 0.04 µm (full width at half max; Nikon 10X Plan Fluor, NA 0.3 Laser powers are given in arbitrary units from 1 to 7 corresponding to 15 ± 1 µW, 107 ± 14 µW, 292 ± 42 µW, 762 ± 105 µW, 1433 ± 49 µW, 1729 ± 165 µW and 1660 ± 163 µW at the objective (n=5 measurements). All illumination spots were placed at approximately 40 µm into the ML at the slice surface. Stimulation pulses were of 20 ms duration.

Light Intensity distribution: To measure the light intensity distribution throughout a slice the setup was modified to image the slice from below while the laser beam was focused to its surface (**Fig. S1C-F**). This was achieved by focusing a surgical Microscope with 36x magnification (M695, Leica Microsystems, Wetzlar, Germany) to the lower slice surface. Images were taken with a CCD camera (Nikon D60). Acute sections of 100, 150, 200, 250, 300 and 350 µm thickness were cut from Prox1-ChR-eYPF mice as described above. The laser was focused to the surface of the slice in the molecular layer and an image was taken at every laser power (P = 1 to 7 AU). The stage was moved for every image to avoid bleaching or phototoxicity. Linear profiles of the resulting isometric light distribution were measured in several directions and averaged to obtain an x profile per section. The x-profiles of slices of different thickness were then stacked to obtain the xz-profile. Values below 100 µm depth were obtained through fitting a Gaussian function in x-direction at 100 µm depth and an exponential function in z-direction. Complete three-dimensional intensity profiles of three different locations of two slices within the dentate molecular layer were averaged.

Calculation of the Optogenetically Activated Cell Fraction: To assess the active fraction of GCs, approximately two GCs were recorded in cell-attached mode in each slice in which an

bioRxiv preprint doi: https://doi.org/10.1101/813188; this version posted October 21, 2019. The copyright holder for this preprint (which was not certified by peer review) is the author/funder, who has granted bioRxiv a license to display the preprint in perpetuity. It is made available under aCC-BY-NC 4.0 International license.

IPSC was recorded. Illumination spots were placed along the GC layer at 100 µm intervals (**Fig. S1**). The entire profile was probed in triplicate with 1 s intervals between individual locations. When the stimulation spot was in sufficient proximity to the recorded cell clear APs were generally visible (in 25 of 26 cells), and otherwise could be induced through simultaneous cell attached depolarization. Cell-attached spikes were detected by automatic thresholding at 6x standard deviation of the baseline. The spatial profile of firing probabilities, centered on the recorded cells, was averaged within each section. To test if cell activation properties differed between blades the maximum firing probabilities (at P = 7) as well as the slopes (increase in firing probability from P = 1 to 7) when simply averaging over all location of a given cell were compared by t-test (n=7 sections per blade, p = 0.490 and 0.684 for max. AP probability and slope, respectively). Since no difference was observed a single firing probability distribution as a function of the distance along the GC layer (x – distance) was calculated for each power (**Fig. S1B,** n = 14 sections, 7 per blade). However, the firing probability of cells in the vicinity of the illumination spot is likely to increase not only as a function of the laser power and spread at the surface, but also of the penetration depth of the light cone. In order to calculate the firing probabilities throughout the slice, the firing probability distribution at the surface was related to the measured light intensity distribution throughout the slice (**Fig. S1C-F**; see above) utilizing a 'virtual distance' measure. Since cells were measured at random distances from the molecular layer border, the light intensity distribution, like the firing probabilities were collapsed to two dimensions, x-distance along the GC layer and z-distance with increasing slice depth. The 'virtual distance' was calculated as the mean distance from a given slice-surface pixel to all other pixels of the light intensity distribution weighted by the intensity within those pixels (**Fig. S1G**). Assigning the firing probabilities of pixels at the slice surface to their respective virtual distance yields the firing probability distribution as a function of virtual distance, which was well approximated by a gaussian fit (**Fig. S1H**). This fit was used to also calculate the firing probabilities of pixels/cells deeper in the slice using the measured light intensity distribution as input. The active cell fraction then corresponds simply to the mean firing probability throughout the slice.

bioRxiv preprint doi: https://doi.org/10.1101/813188; this version posted October 21, 2019. The copyright holder for this preprint (which was not certified by peer review) is the author/funder, who has granted bioRxiv a license to display the preprint in perpetuity. It is made available under aCC-BY-NC 4.0 International license.

This calculation is independent of the size and number of GC and was performed for every power individually. We noted that a large fraction of the recorded spikes occurred with larger latency than the typical IPSC following the beginning of the 20 ms stimulation pulse (**Fig. S1I**, example from a single slice). Since only APs preceding the IPSC can participate in its recruitment, we calculated the fraction of total spikes which preceded mean IPSC latency for every power, and fitted the resulting relation with an exponential function (**Fig. S1J**). All active cell fractions were corrected by this factor (**Fig. S1J**, bottom). Note that this does not take account of the disynaptic delay between mossy fiber output and GC input, thereby potentially slightly overestimating the true recruiting population. For comparison, the active cell fraction was also computed with alternative assumptions about the decay of the firing probability with increasing slice depth. If no firing probability decay with increasing depth is assumed, the active cell fraction throughout the slice is given simply by the average of the measured firing probabilities at the slice surface (**Fig. S1K**, upper grey dashed line). Alternatively, the firing probability decay with depth was assumed to be identical to the measured decay along the slice surface (isometric firing probability distribution; **Fig. S1K**, lower grey dashed line). In this case, Gaussian functions were fit to the probability distributions at the surface and these Gaussian functions were then assumed to extend also in the z-dimension. The active GC fraction was then calculated by numerical integration under the two dimensional Gaussian (with the bounds from 0 to 350 µm in z and -888 to 888 µm in x, which corresponds to the mean GC layer length) normalized to the same area with a uniform firing probability of one. The best estimate of the active GC fraction, incorporating light intensity measurements (**Fig. S1K**, black line), was within these upper and lower bound estimates.

Comparison of Focal and Global Activation:, To globally activate the GC population a multimode light fiber (BF-22, Thorlabs, New Jersey, USA) coupled to a 473 nm laser (Omicron Phoxx, Rodgau-Dudenhofen, Germany) was placed above the slice surface, non-specifically illuminating the entire hippocampus. Analogous to focal stimulations, the activated cell fraction was calculated as the firing probability of individual cells following 20

bioRxiv preprint doi: https://doi.org/10.1101/813188; this version posted October 21, 2019. The copyright holder for this preprint (which was not certified by peer review) is the author/funder, who has granted bioRxiv a license to display the preprint in perpetuity. It is made available under aCC-BY-NC 4.0 International license.

ms pulses. Here no spatial normalization is necessary since cells were sampled from random locations with respect to the light fiber. Firing probabilities for the focal stimulation in these sections was calculated as the simple average of all stimulation locations.

Spatial distribution of feedback inhibition: The same stimulation paradigm which was used to assess cell activation was used to assess the spatial distribution of feedback inhibition. For individual cells, IPSCs at each location and power were averaged. The entire profile was normalized to the largest measured IPSC of that cell, independent of the power and stimulation location at which it occurred. For analysis, all IPSC profiles were spatially aligned to the recorded cells. The mean distance to apex ± one standard deviation was 356 ± 163 µm and 322 ± 97 µm for cells from the superior and inferior blade respectively (n = 8 cells in each blade). In order to test whether there were any distinct effects of the apex, such as a steep decay of inhibition, which would be masked by alignment to the recorded cells, we also aligned the profiles to the apex (not shown). However, no such effects were visible. To analyze the saturated IPSC profiles, normalized IPSC amplitudes from P=5 to 7 were averaged for each cell. In order to analyze the effects of local versus remote stimulation for each blade a distance was chosen such that each remote location was still within the DG but in the other blade (800 µm from the recorded cell). Normalized IPSCs of the three locations surrounding the recorded cell or this remote location were averaged within each power to obtain the IPSC amplitudes for further analysis. The cell fraction required for the activation of a half-maximal IPSC in each section was assessed for each cell by linear interpolation between the measured values. Since no differences were found between superior and inferior inhibition, recordings of both blades were pooled to analyze the kinetic properties of IPSCs. All parameters were calculated on the multiple trials of individual cells. The latency was measured as the time from the beginning of the pulse to when the IPSC superseded 6 fold standard deviation of the baseline. The jitter was calculated as the standard deviation of these latencies for individual cells. The rise time was calculated as the mean 20 to 80 rise time of each cell and the decay time constant was obtained from an exponential fit to the decaying phase of the compound IPSC.

bioRxiv preprint doi: https://doi.org/10.1101/813188; this version posted October 21, 2019. The copyright holder for this preprint (which was not certified by peer review) is the author/funder, who has granted bioRxiv a license to display the preprint in perpetuity. It is made available under aCC-BY-NC 4.0 International license.

Hilar recordings: Intrinsic properties of hilar cells were quantified based on 4.6s long depolarizing current steps or 500ms hyperpolarizing current steps. AP threshold and fast AHP amplitude were measured from the first AP in the first current step in which an AP occurred within the first 10ms. Clustering fraction and mean AP time were calculated from the current injection that elicited the maximum average AP frequency. The Clustering fraction represents the fraction of APs that occur within 60ms before or after another AP [31]. Mean AP time was calculated as the mean AP time point normalized to the duration of the current injection (4.6s). Input resistance was calculated as the slope of the IO curve from the hyperpolarizing current ladder. Cells were manually classified as mossy cells or interneurons based on these intrinsic properties. To objectively confirm classification we performed unsupervised k-means clustering using scikit-learn [94]. For clustering all six measures were normalized by mean and variance. Two cells with conflicting classification were not included in further analysis.

After recording, slices were fixed for 1h in 4% PFA and stored overnight in 0.25% PBS-T at room temperature. The following day they were transferred to PBS for short term storage or immediately stained. For biocytin staining sections were washed with PBS and incubated with Streptavidin-Alexa-Fluor-555 Conjugate (Invitrogen, S32355), 1:1000 in 0.25% PBS-T overnight at 4°C. The following day they were co-stained with DAPI 1:1000 in PBS for 30 minutes and mounted with Aqua-Poly/Mount. Cells were imaged with the Leica SP8 Confocal Microscope of the Microscopy Core Facility at the University Clinic Bonn using a 40x water immersion objective.

Short term dynamics: Short term dynamics of GCs and hilar cells were assessed using antidromic electrical or optogenetic stimulation at minimal power (the smallest stimulation power that yielded reliable responses). Trains of 10 pulses at 1, 10, 30, 50Hz were delivered in triplicate and averaged (excluding sweeps with action currents for hilar cells). In all GCs and a subset of hilar cells we confirmed that PSCs could be blocked by at least 90% with

bioRxiv preprint doi: https://doi.org/10.1101/813188; this version posted October 21, 2019. The copyright holder for this preprint (which was not certified by peer review) is the author/funder, who has granted bioRxiv a license to display the preprint in perpetuity. It is made available under aCC-BY-NC 4.0 International license.

40µM CNQX + 50µM D-APV (n=12, 23 for GCs and hilar cells respectively). Facilitation indices were obtained by normalizing the average of the last three PSC peaks to the first.

To test for differential dynamics between local and remote inhibition analogous trains of optogenetic 20 ms pulses at powers below saturation (usually P=2 for local inhibition and P=3 for remote inhibition) were delivered. For each power and frequency five repeats were recorded and averaged. AP probabilities were assessed by cell-attached recordings with the stimulation site close to the recorded cell. Cell-attached spikes were detected by automatic thresholding as above.

Voltage escape estimation model.

A simple multicompartmental passive 'ball and stick' model with number of segments following the d_lambda rule[95] and passive properties Ra = 181 Ωcm, Cm = 1 uFcm^{-2} and a leak conductance = 0.0002 Scm^{-2}, which gave an Rin of 165 MΩ, were adopted from [95,96]. A soma (20 µm diameter) contained one dendrite (3 µm diameter, 200 µm length) with an alpha synapse point mechanism (Erev -90mV) placed at 180 µm from the soma. The range of synaptic conductances (0.1 – 50 nS; adopted from [97]) elicited IPSC amplitudes in the model, which covered the range of somatic IPSC amplitudes that were experimentally measured (3pA – 1nA). Voltage clamp experiments were simulated using a single electrode point mechanism at the soma (Rs 5 MOhms, to model a Rs of 15 MΩ compensated 70%) with a holding potential of 0 mV. The transfer (Zc) and input impedance (Zn) were determined from the model and used to calculate the actual peak IPSC amplitude at the soma for a given synaptic conductance. Simulations were run in the Neuron 7.5 simulation environment.

Biophysically Realistic Dentate Gyrus Lamella Model: Simulations were run in python 2.7.with NEURON 7.4 [95] on Windows 7/10. We created a generic python-NEURON interface (ouropy, Daniel Müller) which wraps NEURON's python module, into which we ported the conductance based DG model by [56]. Model code is available at https://github.com/danielmuellernai/pyDentate.

bioRxiv preprint doi: https://doi.org/10.1101/813188; this version posted October 21, 2019. The copyright holder for this preprint (which was not certified by peer review) is the author/funder, who has granted bioRxiv a license to display the preprint in perpetuity. It is made available under aCC-BY-NC 4.0 International license.

We first tuned the original model to capture our experimentally determined properties in the most parsimonious way. During tuning we also updated some model properties to better reflect current data and our experimental paradigm in an individual DG lamella:

We introduced a T-type Ca^{2+} channel mechanism into MCs to more realistically reflect the depolarizing envelope at the onset of a positive current step observed in real MCs. Furthermore, while the original model placed the perforant path input at the distal dendrite of GCs, we moved all perforant path synapses to the middle compartment of the dendrite. In order to be able to capture the results of convergent and divergent synaptic inputs in sufficient resolution to produce the empirically observed activity gradations, we up-scaled cell numbers by a factor of four. To model space, we assumed all cell types to be spread out on a 2mm DG lamella. Since MCs project to GCs primarily outside the lamellar plane, we removed the MC to GC connection. To allow patterned PP input we adapted PP input specifications from [57].

We then proceeded in a first phase of model adjustment, and adapted several parameters to reproduce our in vitro findings regarding spatial and temporal feedback inhibition (**Supplementary Table 2**). To model frequency dependent facilitation on mossy fiber outputs, we implemented a simple frequency dependent synapse model (tmgsyn) [98], and matched the facilitation time constant as well as the decay time constants of individual PSCs to our experimental observations. As in the original model, each cell gives rise to a fixed number of synaptic connections which are spatially restricted to a target pool of adjacent cells. We tuned the size and spatial extent of this target pool to reproduce our spatial data. To provide local inhibition we implemented a 'local' interneuron type (BC), whose inputs and outputs were spatially restricted to an ~600µm area (as described by [54]). To provide global inhibition we implemented a second class of inhibitory interneurons (HC) whose inputs and outputs connect to GCs independent of space. This simple formulation allowed us to reproduce the recruitment curves seen for local, remote and global GC activation paradigms. To achieve plausible activity levels, we further adapted synaptic weights similar to [57]. We call

bioRxiv preprint doi: https://doi.org/10.1101/813188; this version posted October 21, 2019. The copyright holder for this preprint (which was not certified by peer review) is the author/funder, who has granted bioRxiv a license to display the preprint in perpetuity. It is made available under aCC-BY-NC 4.0 International license.

the network incorporating both spatially restricted BC synapses and mossy fiber facilitation the full tuned network. To isolate the contribution of intrinsic GC properties to pattern separation we created a disinhibited network by setting the synaptic weight from all interneurons to zero. We also isolated feedforward inhibition by decreasing the mossy fiber to interneuron synaptic weight to zero. To evaluate the effect of spatially constrained inhibition, we created a global network, where the target pool of all interneuron was the entire GC population. To evaluate the effect of mossy fiber facilitation we set the facilitation time constant to zero, effectively eliminating facilitation. Details on the model parameters are summarized in **Supplementary Table 2**).

To study pattern separation, we generated 400 PP inputs. Each PP synapsed onto 100 randomly chosen GCs with the spatial connection probability being governed by a gaussian probability distribution with standard deviation 1mm and random peak position, modeling a full, nearly uniform input connectivity of individual afferents [82]. To generate theta modulated spike patterns we used the inhomogeneous poisson generator from Elephant 0.5.0-Electrophysiology-Analysis-Toolkit with a 10 Hz (theta) sinusoidal rate profile with a peak of 100 Hz, a minimum of 0 Hz and a duration of 600 ms. To generate input patterns with varying overlap from PP afferents i = 1 to 400, we activated afferents i to i+23 in increments of i = 1 per run. We performed 25 runs for each condition resulting in 300 unique comparisons, excluding self-comparisons. The random seed was held constant between different runs of the same condition, resulting in differing input patterns being fed into the same network. All randomness was generated with the python module numpy.random.

To quantify pattern similarity we used Pearson's product moment correlation coefficient R of the population rate vectors for input and output patterns. The population rate vector refers to the vector of the mean firing rates of all cells in the population within the entire 600 ms simulation, or 100 or 33 ms time windows for the time resolved analyses. All statistical analyses of the model were performed with n=7 different random network seeds.

bioRxiv preprint doi: https://doi.org/10.1101/813188; this version posted October 21, 2019. The copyright holder for this preprint (which was not certified by peer review) is the author/funder, who has granted bioRxiv a license to display the preprint in perpetuity. It is made available under aCC-BY-NC 4.0 International license.

To compute full pattern separation effects (Fig. 6D) we calculated the mean R_{out} within R_{in} bins of 0.1 and measured the area to the unity line (computed as the mean of the binwise R_{in} – R_{out} differences). To compute isolated pattern separation effects of specific manipulations we subtracted the respective R_{out} values with and without the manipulation, thereby obtaining a ΔR_{out} value for each individual R_{in}. We then again computed the bin-wise mean and quantified the area under the curve, yielding the mean ΔR_{out} analogous to the full effects. Note, that the sequence of averaging and subtracting is irrelevant, and was inverted only to match the figure panels. Data are displayed as mean ± SEM for each R_{in} bin (**Fig. 6E, G**). The coefficient of variance (CoV) was calculated by normalizing the standard deviation of ΔR_{out} within each bin by the mean of that bin, and then averaging over bins, analogous to the previous analyses. However, only bins within $0.2<R_{in}<0.8$ were included, since at the borders very small means led to unreliable results. ΔCoV represents the difference between the mean CoV of the global (or nonfacilitating) and the tuned network models. For the temporally resolved pattern separation analysis all measures were computed as above, but on population vector correlations within 100ms time bins.

Statistics and Data Analysis: Analyses were performed using ImageJ, Microsoft Excel, Python and Igor Pro. Fits were performed using Igor Pro. Statistical analyses were performed using GraphPad Prism 6 or Igor Pro. Comparisons were two-tailed whenever applicable. Replicates refer to cells unless otherwise indicated (slices for imaging experiments and network seeds for modeling data). Statistical significance in Analysis of Variance (ANOVA) is indicated by §. F-values and degrees of freedom are given as F(DFn, DFd). When ANOVAs were followed by specific comparisons these are indicated by asterisks, where *P<.05, **P<.01 and ***P<0.001. Bargraphs and XY plots show means where error bars indicate standard error of the mean. In boxplots error bars represent the data range and boxes the upper and lower quartiles and the median.

bioRxiv preprint doi: https://doi.org/10.1101/813188; this version posted October 21, 2019. The copyright holder for this preprint (which was not certified by peer review) is the author/funder, who has granted bioRxiv a license to display the preprint in perpetuity. It is made available under aCC-BY-NC 4.0 International license.

References

1. Cayco-Gajic, N. A. & Silver, R. A. Re-evaluating Circuit Mechanisms Underlying Pattern Separation. *Neuron* **101**, 584–602 (2019).

2. Marr, D. Simple memory: a theory for archicortex. *Philos. Trans. R. Soc. Lond. B. Biol. Sci.* **262**, 23–81 (1971).

3. McNaughton, B. L. & Morris, R. G. M. Hippocampal synaptic enhancement and information storage within a distributed memory system. *Trends Neurosci.* **10**, 408–415 (1987).

4. Rolls, E. T. The mechanisms for pattern completion and pattern separation in the hippocampus. *Front. Syst. Neurosci.* **7**, 74 (2013).

5. Krueppel, R. Dendritic integration in hippocampal dentate gyrus granule cells. (2010).

6. Cayco-Gajic, N. A., Clopath, C. & Silver, R. A. Sparse synaptic connectivity is required for decorrelation and pattern separation in feedforward networks. *Nat. Commun.* **8**, 1116 (2017).

7. Braganza, O. *Proxyeconomics, An agent based model of Campbell's law in competitive societal systems*. (2018).

8. Wick, S. D., Wiechert, M. T., Friedrich, R. W. & Riecke, H. Pattern orthogonalization via channel decorrelation by adaptive networks. *J. Comput. Neurosci.* **28**, 29–45 (2010).

9. Wiechert, M. T., Judkewitz, B., Riecke, H. & Friedrich, R. W. Mechanisms of pattern decorrelation by recurrent neuronal circuits. *Nat. Neurosci.* **13**, 1003–1010 (2010).

10. Lin, A. C., Bygrave, A. M., de Calignon, A., Lee, T. & Miesenböck, G. Sparse, decorrelated odor coding in the mushroom body enhances learned odor discrimination. *Nat. Neurosci.* **17**, 559–68 (2014).

11. Papadopoulou, M., Cassenaer, S., Nowotny, T. & Laurent, G. Normalization for sparse

bioRxiv preprint doi: https://doi.org/10.1101/813188; this version posted October 21, 2019. The copyright holder for this preprint (which was not certified by peer review) is the author/funder, who has granted bioRxiv a license to display the preprint in perpetuity. It is made available under aCC-BY-NC 4.0 International license.

encoding of odors by a wide-field interneuron. *Science* **332**, 721–5 (2011).

12. Leutgeb, J. J. K. J., Leutgeb, S., Moser, M. M.-B. M. & Moser, E. E. I. Pattern separation in the dentate gyrus and CA3 of the hippocampus. *Science (80-.).* **315**, 961–6 (2007).

13. Neunuebel, J. P. & Knierim, J. J. CA3 Retrieves Coherent Representations from Degraded Input: Direct Evidence for CA3 Pattern Completion and Dentate Gyrus Pattern Separation. *Neuron* **81**, 416–427 (2014).

14. Leal, S. L. & Yassa, M. A. Integrating new findings and examining clinical applications of pattern separation. *Nat. Neurosci.* **21**, 163–173 (2018).

15. Gilbert, P. E., Kesner, R. P. & Lee, I. Dissociating hippocampal subregions: double dissociation between dentate gyrus and CA1. *Hippocampus* **11**, 626–36 (2001).

16. McHugh, T. J. *et al.* Dentate gyrus NMDA receptors mediate rapid pattern separation in the hippocampal network. *Science* **317**, 94–9 (2007).

17. Bakker, A., Kirwan, C. B., Miller, M. & Stark, C. E. L. Pattern separation in the human hippocampal CA3 and dentate gyrus. *Science* **319**, 1640–2 (2008).

18. Berron, D. *et al.* Strong Evidence for Pattern Separation in Human Dentate Gyrus. *J. Neurosci.* **36**, (2016).

19. van Dijk, M. T. & Fenton, A. A. On How the Dentate Gyrus Contributes to Memory Discrimination. *Neuron* **98**, 832-845.e5 (2018).

20. Stefanelli, T., Bertollini, C., Lüscher, C., Muller, D. & Mendez, P. Hippocampal Somatostatin Interneurons Control the Size of Neuronal Memory Ensembles. *Neuron* **89**, 1074–85 (2016).

21. Savanthrapadian, S. *et al.* Synaptic properties of SOM- and CCK-expressing cells in dentate gyrus interneuron networks. *J. Neurosci.* **34**, 8197–209 (2014).

22. Espinoza, C., Guzman, S. J., Zhang, X. & Jonas, P. Parvalbumin+ interneurons obey unique connectivity rules and establish a powerful lateral-inhibition microcircuit in

bioRxiv preprint doi: https://doi.org/10.1101/813188; this version posted October 21, 2019. The copyright holder for this preprint (which was not certified by peer review) is the author/funder, who has granted bioRxiv a license to display the preprint in perpetuity. It is made available under aCC-BY-NC 4.0 International license.

dentate gyrus. *Nat. Commun.* **9**, 4605 (2018).

23. Lysetskiy, M., Földy, C. & Soltesz, I. Long- and short-term plasticity at mossy fiber synapses on mossy cells in the rat dentate gyrus. *Hippocampus* **15**, 691–6 (2005).

24. Kraushaar, U. & Jonas, P. Efficacy and Stability of Quantal GABA Release at a Hippocampal Interneuron-Principal Neuron Synapse. *J. Neurosci.* **20**, 5594–5607 (2000).

25. Hefft, S. & Jonas, P. Asynchronous GABA release generates long-lasting inhibition at a hippocampal interneuron-principal neuron synapse. *Nat. Neurosci.* **8**, 1319–28 (2005).

26. Zhang, W. *et al.* Surviving hilar somatostatin interneurons enlarge, sprout axons, and form new synapses with granule cells in a mouse model of temporal lobe epilepsy. *J. Neurosci.* **29**, 14247–56 (2009).

27. Bartos, M. *et al.* Fast synaptic inhibition promotes synchronized gamma oscillations in hippocampal interneuron networks. *Proc. Natl. Acad. Sci. U. S. A.* **99**, 13222–7 (2002).

28. Harney, S. C. & Jones, M. V. Pre- and postsynaptic properties of somatic and dendritic inhibition in dentate gyrus. *Neuropharmacology* **43**, 584–594 (2002).

29. Yuan, M. *et al.* Somatostatin-positive interneurons in the dentate gyrus of mice provide local- and long-range septal synaptic inhibition. *Elife* **6**, (2017).

30. Yu, J., Swietek, B., Proddutur, A. & Santhakumar, V. Dentate total molecular layer interneurons mediate cannabinoid-sensitive inhibition. *Hippocampus* **25**, 884–9 (2015).

31. Larimer, P. & Strowbridge, B. W. Nonrandom Local Circuits in the Dentate Gyrus. *J. Neurosci.* **28**, 12212–12223 (2008).

32. Ewell, L. & Jones, M. Frequency-tuned distribution of inhibition in the dentate gyrus. *J. Neurosci.* **30**, 12597–607 (2010).

33. Sik, A., Penttonen, M. & Buzsaki, G. Interneurons in the Hippocampal Dentate

bioRxiv preprint doi: https://doi.org/10.1101/813188; this version posted October 21, 2019. The copyright holder for this preprint (which was not certified by peer review) is the author/funder, who has granted bioRxiv a license to display the preprint in perpetuity. It is made available under aCC-BY-NC 4.0 International license.

Gyrus□: an In Vivo Intracellular Study. *Eur. J. Neurosci.* **9**, 573–588 (1997).

34. Freund, T. F. & Buzsáki, G. Interneurons of the hippocampus. *Hippocampus* **6**, 347–470 (1996).

35. Lee, C.-T. *et al.* Causal Evidence for the Role of Specific GABAergic Interneuron Types in Entorhinal Recruitment of Dentate Granule Cells. *Sci. Rep.* **6**, 36885 (2016).

36. Geiger, J. R., Lübke, J., Roth, A., Frotscher, M. & Jonas, P. Submillisecond AMPA receptor-mediated signaling at a principal neuron-interneuron synapse. *Neuron* **18**, 1009–23 (1997).

37. Liu, Y.-C., Cheng, J.-K. & Lien, C.-C. Rapid dynamic changes of dendritic inhibition in the dentate gyrus by presynaptic activity patterns. *J. Neurosci.* **34**, 1344–57 (2014).

38. Sambandan, S., Sauer, J.-F. J.-F., Vida, I. & Bartos, M. Associative plasticity at excitatory synapses facilitates recruitment of fast-spiking interneurons in the dentate gyrus. *J. Neurosci.* **30**, 11826–37 (2010).

39. Dasgupta, D. & Sikdar, S. K. Calcium permeable AMPA receptor-dependent long lasting plasticity of intrinsic excitability in fast spiking interneurons of the dentate gyrus decreases inhibition in the granule cell layer. *Hippocampus* **25**, 269–285 (2015).

40. Hsu, T.-T., Lee, C.-T., Tai, M.-H. & Lien, C.-C. Differential Recruitment of Dentate Gyrus Interneuron Types by Commissural Versus Perforant Pathways. *Cereb. Cortex* **26**, bhv127- (2015).

41. Trimper, J. B., Galloway, C. R., Jones, A. C., Mandi, K. & Manns, J. R. Gamma Oscillations in Rat Hippocampal Subregions Dentate Gyrus, CA3, CA1, and Subiculum Underlie Associative Memory Encoding. *Cell Rep.* **21**, 2419–2432 (2017).

42. Pernía-Andrade, A. J. & Jonas, P. Theta-gamma-modulated synaptic currents in hippocampal granule cells in vivo define a mechanism for network oscillations. *Neuron* **81**, 140–52 (2014).

43. Hsiao, Y.-T., Zheng, C. & Colgin, L. L. Slow gamma rhythms in CA3 are entrained by

bioRxiv preprint doi: https://doi.org/10.1101/813188; this version posted October 21, 2019. The copyright holder for this preprint (which was not certified by peer review) is the author/funder, who has granted bioRxiv a license to display the preprint in perpetuity. It is made available under aCC-BY-NC 4.0 International license.

slow gamma activity in the dentate gyrus. *J. Neurophysiol.* jn.00499.2016 (2016). doi:10.1152/jn.00499.2016

44. Sasaki, T. *et al.* Dentate network activity is necessary for spatial working memory by supporting CA3 sharp-wave ripple generation and prospective firing of CA3 neurons. *Nat. Neurosci.* **21**, 258–269 (2018).

45. Rolls, E. T. Pattern separation, completion, and categorisation in the hippocampus and neocortex. *Neurobiol. Learn. Mem.* **129**, 4–28 (2016).

46. Myers, C. E. & Scharfman, H. E. A role for hilar cells in pattern separation in the dentate gyrus: a computational approach. *Hippocampus* **19**, 321–337 (2009).

47. Doherty, J. & Dingledine, R. Differential Regulation of Synaptic Inputs to Dentate Hilar Border Interneurons by Metabotropic Glutamate Receptors. 2903–2910 (1998).

48. Toth, K., Suares, G., Lawrence, J. J., Philips-Tansey, E. & McBain, C. J. Differential mechanisms of transmission at three types of mossy fiber synapse. *J. Neurosci.* **20**, 8279–89 (2000).

49. Bischofberger, J., Engel, D., Li, L., Geiger, J. R. P. & Jonas, P. Patch-clamp recording from mossy fiber terminals in hippocampal slices. *Nat. Protoc.* **1**, 2075–81 (2006).

50. Kapfer, C., Glickfeld, L., Atallah, B. & Scanziani, M. Supralinear increase of recurrent inhibition during sparse activity in the somatosensory cortex. *Nat. Neurosci.* **10**, 743–53 (2007).

51. Miles, R. Synaptic excitation of inhibitory cells by single CA3 hippocampal pyramidal cells of the guinea-pig in vitro. *J. Physiol.* **428**, 61–77 (1990).

52. Silberberg, G. & Markram, H. Disynaptic inhibition between neocortical pyramidal cells mediated by Martinotti cells. *Neuron* **53**, 735–46 (2007).

53. Jouhanneau, J.-S., Kremkow, J. & Poulet, J. F. A. Single synaptic inputs drive high-precision action potentials in parvalbumin expressing GABA-ergic cortical neurons in vivo. *Nat. Commun.* **9**, 1540 (2018).

bioRxiv preprint doi: https://doi.org/10.1101/813188; this version posted October 21, 2019. The copyright holder for this preprint (which was not certified by peer review) is the author/funder, who has granted bioRxiv a license to display the preprint in perpetuity. It is made available under aCC-BY-NC 4.0 International license.

54. Strüber, M., Jonas, P. & Bartos, M. Strength and duration of perisomatic GABAergic inhibition depend on distance between synaptically connected cells. *Proc. Natl. Acad. Sci. U. S. A.* **112**, 1220–1225 (2015).

55. Pothmann, L. *et al.* Function of inhibitory micronetworks is spared by Na+ channel-acting anticonvulsant drugs. *J. Neurosci.* **34**, 9720–35 (2014).

56. Santhakumar, V., Aradi, I. & Soltesz, I. Role of mossy fiber sprouting and mossy cell loss in hyperexcitability: a network model of the dentate gyrus incorporating cell types and axonal topography. *J. Neurophysiol.* **93**, 437–53 (2005).

57. Yim, M. Y., Hanuschkin, A. & Wolfart, J. Intrinsic rescaling of granule cells restores pattern separation ability of a dentate gyrus network model during epileptic hyperexcitability. *Hippocampus* **25**, 297–308 (2015).

58. Madar, A. D., Ewell, L. A. & Jones, M. V. Temporal pattern separation in hippocampal neurons through multiplexed neural codes. *PLOS Comput. Biol.* **15**, e1006932 (2019).

59. Buzsáki, G. Neural syntax: cell assemblies, synapsembles, and readers. *Neuron* **68**, 362–85 (2010).

60. de Almeida, L., Idiart, M. & Lisman, J. A second function of gamma frequency oscillations: an E%-max winner-take-all mechanism selects which cells fire. *J. Neurosci.* **29**, 7497–7503 (2009).

61. Rolls, E. T. A computational theory of episodic memory formation in the hippocampus. *Behav. Brain Res.* **215**, 180–96 (2010).

62. Hunsaker, M. R., Rosenberg, J. S. & Kesner, R. P. The role of the dentate gyrus, CA3a,b, and CA3c for detecting spatial and environmental novelty. *Hippocampus* **18**, 1064–1073 (2008).

63. Schmidt, B., Marrone, D. F. & Markus, E. J. Disambiguating the similar: the dentate gyrus and pattern separation. *Behav. Brain Res.* **226**, 56–65 (2012).

64. Rolls, E. T. & Treves, A. Neural Networks and Brain Function - Chapter 4: Competitive

bioRxiv preprint doi: https://doi.org/10.1101/813188; this version posted October 21, 2019. The copyright holder for this preprint (which was not certified by peer review) is the author/funder, who has granted bioRxiv a license to display the preprint in perpetuity. It is made available under aCC-BY-NC 4.0 International license.

networks. 54–74 (1998).

65. Trappenberg, T. P. Fundamentals of computational neuroscience. *Oxford Univ. Press* (2010). doi:10.5860/CHOICE.40-2778

66. Hendrickson, P. J., Yu, G. J., Song, D. & Berger, T. W. Interactions between Inhibitory Interneurons and Excitatory Associational Circuitry in Determining Spatio-Temporal Dynamics of Hippocampal Dentate Granule Cells: A Large-Scale Computational Study. *Front. Syst. Neurosci.* **9**, 155 (2015).

67. Chavlis, S., Petrantonakis, P. C. & Poirazi, P. Dendrites of dentate gyrus granule cells contribute to pattern separation by controlling sparsity. *Hippocampus* **27**, 89–110 (2017).

68. Hummos, A., Franklin, C. C. & Nair, S. S. Intrinsic mechanisms stabilize encoding and retrieval circuits differentially in a hippocampal network model. *Hippocampus* **24**, 1430–1448 (2014).

69. Skaggs, W. E., McNaughton, B. L., Wilson, M. a & Barnes, C. a. Theta phase precession in hippocampal neuronal populations and the compression of temporal sequences. *Hippocampus* **6**, 149–72 (1996).

70. Mizuseki, K., Sirota, A., Pastalkova, E. & Buzs?ki, G. Theta Oscillations Provide Temporal Windows for Local Circuit Computation in the Entorhinal-Hippocampal Loop. *Neuron* **64**, 267–280 (2009).

71. Rangel, L. M., Chiba, A. A. & Quinn, L. K. Theta and beta oscillatory dynamics in the dentate gyrus reveal a shift in network processing state during cue encounters. *Front. Syst. Neurosci.* **9**, 96 (2015).

72. Berke, J. D., Hetrick, V., Breck, J. & Greene, R. W. Transient 23-30 Hz oscillations in mouse hippocampus during exploration of novel environments. *Hippocampus* **18**, 519–529 (2008).

73. Barth, A. M., Domonkos, A., Fernandez-Ruiz, A., Freund, T. F. & Varga, V.

bioRxiv preprint doi: https://doi.org/10.1101/813188; this version posted October 21, 2019. The copyright holder for this preprint (which was not certified by peer review) is the author/funder, who has granted bioRxiv a license to display the preprint in perpetuity. It is made available under aCC-BY-NC 4.0 International license.

Hippocampal Network Dynamics during Rearing Episodes. *Cell Rep.* **23**, 1706–1715 (2018).

74. Szabo, G. G. *et al.* Extended Interneuronal Network of the Dentate Gyrus. *Cell Rep.* **20**, 1262–1268 (2017).

75. Sahay, A. *et al.* Increasing adult hippocampal neurogenesis is sufficient to improve pattern separation. *Nature* **472**, 466–70 (2011).

76. Clelland, C. D. *et al.* A functional role for adult hippocampal neurogenesis in spatial pattern separation. *Science* **325**, 210–3 (2009).

77. Aimone, J. B., Deng, W. & Gage, F. H. Resolving new memories: a critical look at the dentate gyrus, adult neurogenesis, and pattern separation. *Neuron* **70**, 589–96 (2011).

78. Li, L. *et al.* Silent synapses generate sparse and orthogonal action potential firing in adult-born hippocampal granule cells. *Elife* **6**, (2017).

79. Severa, W., Parekh, O., James, C. D. & Aimone, J. B. A Combinatorial Model for Dentate Gyrus Sparse Coding. *Neural Comput.* **29**, 94–117 (2017).

80. Temprana, S. G. *et al.* Delayed Coupling to Feedback Inhibition during a Critical Period for the Integration of Adult-Born Granule Cells. *Neuron* **85**, 116–131 (2015).

81. Pouille, F. & Scanziani, M. Routing of spike series by dynamic circuits in the hippocampus. *Nature* **429**, 717–23 (2004).

82. Tamamaki, N. & Nojyo, Y. Projection of the entorhinal layer II neurons in the rat as revealed by intracellular pressure-injection of neurobiotin. *Hippocampus* **3**, 471–480 (1993).

83. Tamamaki, N. Organization of the entorhinal projection to the rat dentate gyrus revealed by Dil anterograde labeling. *Exp. brain Res.* **116**, 250–8 (1997).

84. Feldt Muldoon, S., Soltesz, I. & Cossart, R. Spatially clustered neuronal assemblies comprise the microstructure of synchrony in chronically epileptic networks. *Proc. Natl. Acad. Sci. U. S. A.* **110**, 3567–72 (2013).

bioRxiv preprint doi: https://doi.org/10.1101/813188; this version posted October 21, 2019. The copyright holder for this preprint (which was not certified by peer review) is the author/funder, who has granted bioRxiv a license to display the preprint in perpetuity. It is made available under aCC-BY-NC 4.0 International license.

85. Chawla, M. K. *et al.* Sparse, environmentally selective expression of Arc RNA in the upper blade of the rodent fascia dentata by brief spatial experience. *Hippocampus* **15**, 579–86 (2005).

86. Alme, C. B. *et al.* Hippocampal granule cells opt for early retirement. *Hippocampus* **20**, 1109–23 (2010).

87. Andrews-Zwilling, Y. *et al.* Hilar GABAergic interneuron activity controls spatial learning and memory retrieval. *PLoS One* **7**, e40555 (2012).

88. Verret, L. *et al.* Inhibitory interneuron deficit links altered network activity and cognitive dysfunction in Alzheimer model. *Cell* **149**, 708–721 (2012).

89. Gillespie, A. K. *et al.* Apolipoprotein E4 Causes Age-Dependent Disruption of Slow Gamma Oscillations during Hippocampal Sharp-Wave Ripples. *Neuron* **90**, 740–51 (2016).

90. Gong, S. *et al.* A gene expression atlas of the central nervous system based on bacterial artificial chromosomes. *Nature* **425**, 917–25 (2003).

91. Gong, S. *et al.* Targeting Cre recombinase to specific neuron populations with bacterial artificial chromosome constructs. *J. Neurosci.* **27**, 9817–23 (2007).

92. Schmidt-Hieber, C., Jonas, P. & Bischofberger, J. Enhanced synaptic plasticity in newly generated granule cells of the adult hippocampus. *Nature* **429**, 184–7 (2004).

93. Garaschuk, O., Milos, R. & Konnerth, A. Targeted bulk-loading of fluorescent indicators for two-photon brain imaging in vivo. *Nat. Protoc.* **1**, 380–6 (2006).

94. Pedregosa, F. *et al.* Scikit-learn: Machine Learning in Python. *J. Mach. Learn. Res.* **12**, 2825–2830 (2011).

95. Carnevale, N. T. & Hines, M. L. *The NEURON Book*. (Cambridge University Press, 2006). doi:10.1017/CBO9780511541612

96. Krueppel, R., Remy, S. & Beck, H. Dendritic integration in hippocampal dentate granule cells. *Neuron* **71**, 512–28 (2011).

bioRxiv preprint doi: https://doi.org/10.1101/813188; this version posted October 21, 2019. The copyright holder for this preprint (which was not certified by peer review) is the author/funder, who has granted bioRxiv a license to display the preprint in perpetuity. It is made available under aCC-BY-NC 4.0 International license.

97. Williams, S. R. & Mitchell, S. J. Direct measurement of somatic voltage clamp errors in central neurons. *Nat. Neurosci.* **11**, 790–798 (2008).

98. Tsodyks, M., Pawelzik, K. & Markram, H. Neural Networks with Dynamic Synapses. *Neural Comput.* **10**, 821–835 (1998).

bioRxiv preprint doi: https://doi.org/10.1101/813188; this version posted October 21, 2019. The copyright holder for this preprint (which was not certified by peer review) is the author/funder, who has granted bioRxiv a license to display the preprint in perpetuity. It is made available under aCC-BY-NC 4.0 International license.

Acknowledgements:

This work was supported by the Deutsche Forschungsgemeinschaft (SFB 1089, ebGluNet), the BONFOR program of the University of Bonn Medical Center, the ERANET Neuron grant 'EpiNet' (to H.B.). We thank Olivia van Ray and Dominik Holtkamp for excellent technical assistance; Thoralf Opitz, Holger Dannenberg, Laura Ewell and Dirk Dietrich for valuable comments and Stefan Remy for access to multi-beam two-photon microscopy. We further acknowledge support by the Microscopy Core Facility of the Medical Faculty.

Author contributions

H.B. and O.B. conceived of the study and wrote the manuscript. D.M. performed hilar experiments, created the computational model and contributed to the manuscript. T.K. contributed technical and analytical expertise and modeled voltage escape errors. All other experiments and analyses were performed by O.B.

Competing interests

The authors declare no competing interests.

bioRxiv preprint doi: https://doi.org/10.1101/813188; this version posted October 21, 2019. The copyright holder for this preprint (which was not certified by peer review) is the author/funder, who has granted bioRxiv a license to display the preprint in perpetuity. It is made available under aCC-BY-NC 4.0 International license.

Supplementary Materials

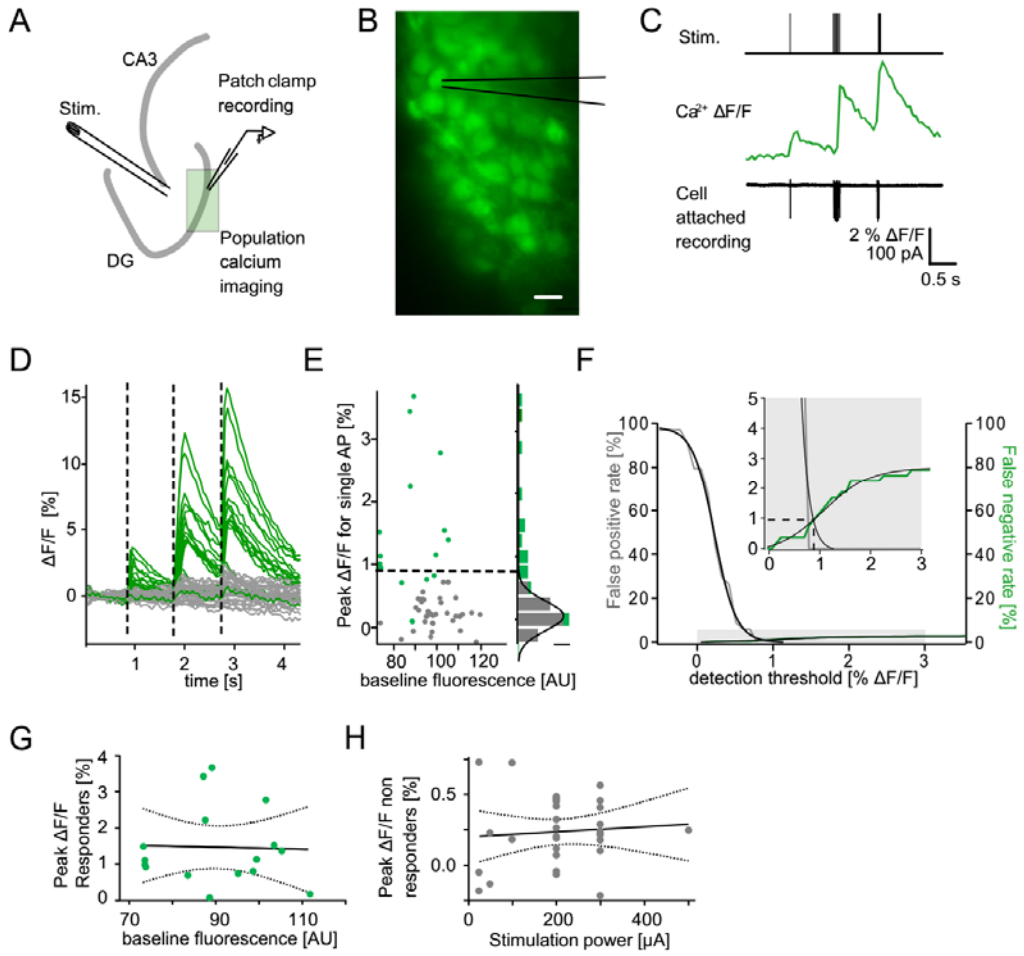

Fig. S1 Detection of single action potential induced calcium transients, A section of the dentate gyrus was loaded with OGB1-AM and imaged with multibeam two-photon microscopy while antidromically eliciting action potentials and recording from individual cells in cell-attached mode. **A)** A schematic illustration of the experimental setup. **B)** Example of OGB1-AM loaded GCs. Scale bar: 10 µm **C)** Cells were stimulated with a single pulse (left) or bursts of 5 pulses at 30 Hz (middle) or 100 Hz (right). Cell attached recordings revealed the exact number of induced action potentials (bottom) which could then be correlated with the intracellular calcium signal (middle). **D)** Superposition of the calcium fluorescence traces of 49 recorded cells constituted of cells identified as responders (green) or non-responders (grey) by cell attached recordings. **E)** Peak ΔF/F for single APs of identified responders and non-responders plotted against their respective baseline fluorescence (left). A histogram of the peak ΔF/F of both groups fitted with a Gaussian distribution of the non-responders (right, scale bar = 5 cells). The dashed line indicates detection threshold at the quadruple standard deviation of this fit (0.94% ΔF/F). **F)** False positive (gray) and false negative (green) rates were plotted as a function of the detection threshold and fitted with sigmoidal functions. A detection threshold of 0.94% leads to exactly equal numbers of false positives and false negatives at a true positive rate of 3% (inset, dashed lines). **G)** To test for potential effects of variable dye loading on detection efficacy, we tested for a correlation between peak ΔF/F of responders and baseline fluorescence intensity ($p>0.05$). **H)** -To test if increasing numbers of responders at increasing stimulation power led to increases of false positives in the densely packed GC layer we correlated peak ΔF/F of non-responders with stimulation power ($p>0.05$). Dashed lines in (G) and (H) represent the 95% confidence intervals of linear regressions.

bioRxiv preprint doi: https://doi.org/10.1101/813188; this version posted October 21, 2019. The copyright holder for this preprint (which was not certified by peer review) is the author/funder, who has granted bioRxiv a license to display the preprint in perpetuity. It is made available under aCC-BY-NC 4.0 International license.

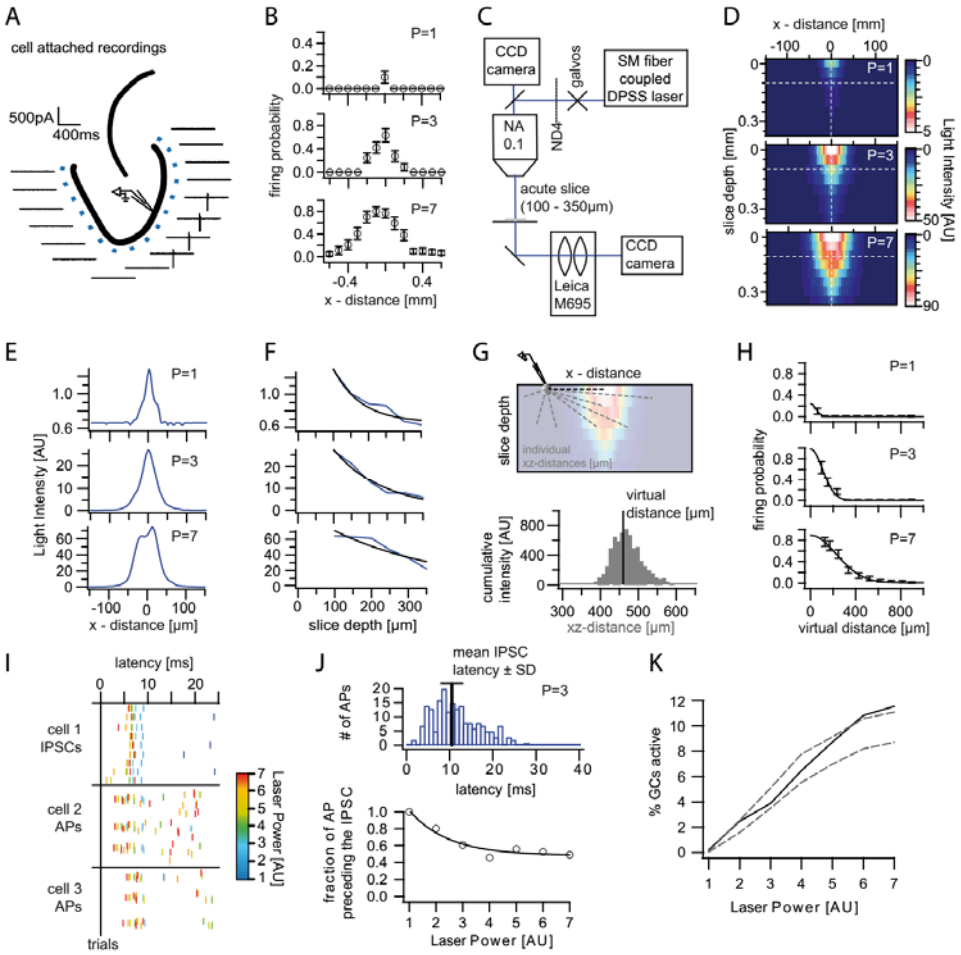

Fig. S2, Optogenetically activated cell fraction. A) Schematic illustration of the experimental setup. Cells were recorded in cell attached mode (2 per slice), while systematically stimulating at varying distances. Traces from a representative trial at P = 3. **B)** Mean firing probability of every location over trials and cells for each laser power (3 example powers shown). **C)** Schematic of the modified setup to record the 3 dimensional light intensity profile in an acute slice. In order to avoid saturation a neutral density filter (ND4) was inserted into the light path. **D)** Cross section of the light intensity profile of the laser spot at increasing slice depth. The dashed white lines indicate the location of the cross sections shown in (E) and (F). Depths below 100 µm were extrapolated from fits to (E) and (F). **G) top,** Illustration of the calculation of the virtual distance for a particular cell/pixel 440µm lateral to the laser focus. The distances between the given cell/pixel and all other pixels (individual xz-distances) were weighted by the intensity at those pixels. **Bottom,** This weighting is illustrated by a histogram displaying the intensities for each respective xz-distance. The virtual distance corresponds to the intensity weighted mean of xz-distances. **H)** The measured firing probabilities were assigned to the respective virtual distances. The resulting firing probability distribution was well approximated by a Gaussian fit (black lines). **I)** Example of the IPSC and AP latencies upon a stimulation pulse from an individual slice. Laser Powers are color coded. **J) Top**, Example Histogram of the distribution of all AP latencies for P = 3 (blue). The black bar indicates the mean IPSC latency ± standard deviation at that power. **Bottom,** The fraction of action potentials that precede the mean IPSC for each power was well approximated by an exponential fit (black line). Light stimulation in (I) and (J) was from 0 to 20 ms. **K) black,** Estimated active cell fraction in the slice calculated from the light intensity profiles in (D) and the virtual firing probability distributions in (H) and corrected by the fraction of APs occurring after the mean IPSC (J). The estimated active cell fraction is identical to the mean firing probability throughout the slice. For comparison the cell fraction was also estimated assuming no firing probability decay with increasing depth (upper grey dashed line) or assuming isometric decay (lower grey dashed line).

bioRxiv preprint doi: https://doi.org/10.1101/813188; this version posted October 21, 2019. The copyright holder for this preprint (which was not certified by peer review) is the author/funder, who has granted bioRxiv a license to display the preprint in perpetuity. It is made available under aCC-BY-NC 4.0 International license.

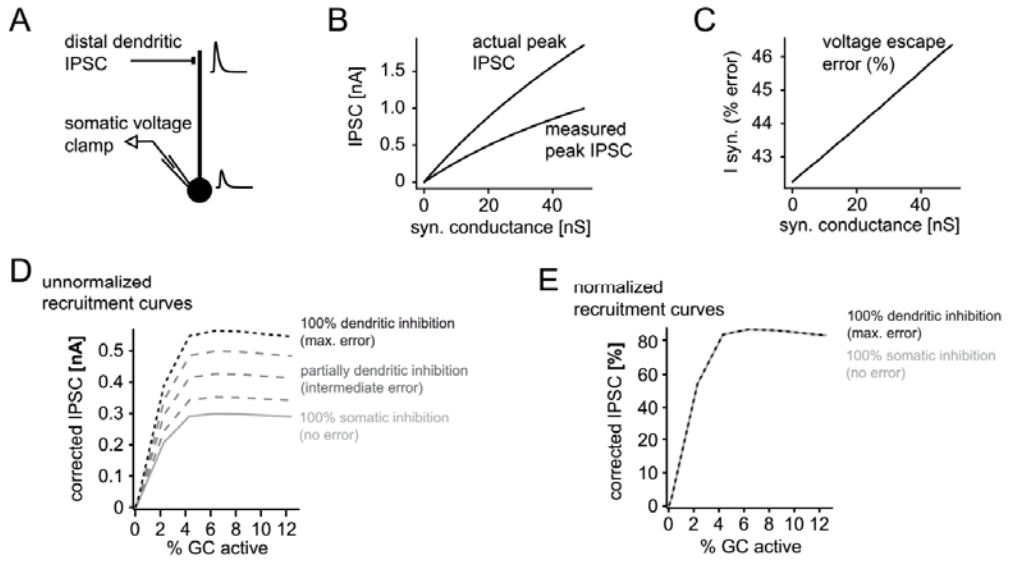

Fig. S3, Error in somatic IPSC measurements with increasing inhibitory conductance. A simple ball and stick model was used to estimate the impact of voltage escape errors for dendritic IPSCs (soma diameter 20um; dendrite diameter and length 3 µm and 200 µm, respectively). To estimate the maximum errors the inhibitory synapse was placed at a distal site (180 µm from the soma) and inhibitory currents were measured using a single electrode voltage-clamp at the soma. **A)** Illustration of the model and an attenuated somatic IPSC measurement. **B,** Peak amplitudes of the measured IPSC over a range of distal synaptic conductances (measured peak IPSC), as well as the actual peak IPSC in the absence of voltage errors, calculated from the transfer and input impedances of the model. **C)** Error in somatically measured peak IPSC as percentage of the actual peak IPSC (I syn, % error) at a given synaptic conductance. Errors in estimating synaptic inhibitory currents were linear. **D,** Illustration of corrected and uncorrected recruitment curves of absolute IPSC amplitudes for varying degrees of voltage error (using data from the recruitment curve in **Fig. 2H**). Note that due to the linearity of voltage escape errors, absolute IPSC amplitudes change, but the saturation point does not. **E)** This is illustrated by the normalized recruitment curves, as shown throughout the manuscript (see i.e. **Fig. 2H**). Note that normalized curves are practically unaffected by voltage escape errors.

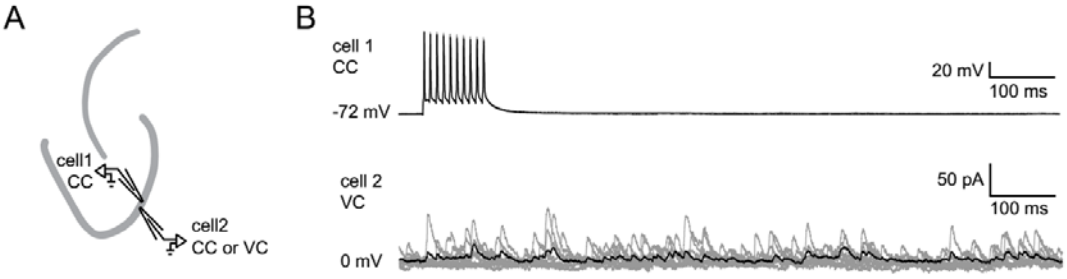

Fig. S4, Absence of single GC induced feedback inhibition. Pairs of juxtaposed GCs (< 100µm distance) were recorded to test for single GC induced feedback inhibition. **A)** Schematic illustration of the experimental setup. **B)** Example of a paired recording where cell 1 is fired at 100 Hz in current clamp mode while cell 2 is recorded in voltage clamp mode in order to detect IPSCs. (gray, 10 individual trials; black, average).

bioRxiv preprint doi: https://doi.org/10.1101/813188; this version posted October 21, 2019. The copyright holder for this preprint (which was not certified by peer review) is the author/funder, who has granted bioRxiv a license to display the preprint in perpetuity. It is made available under aCC-BY-NC 4.0 International license.

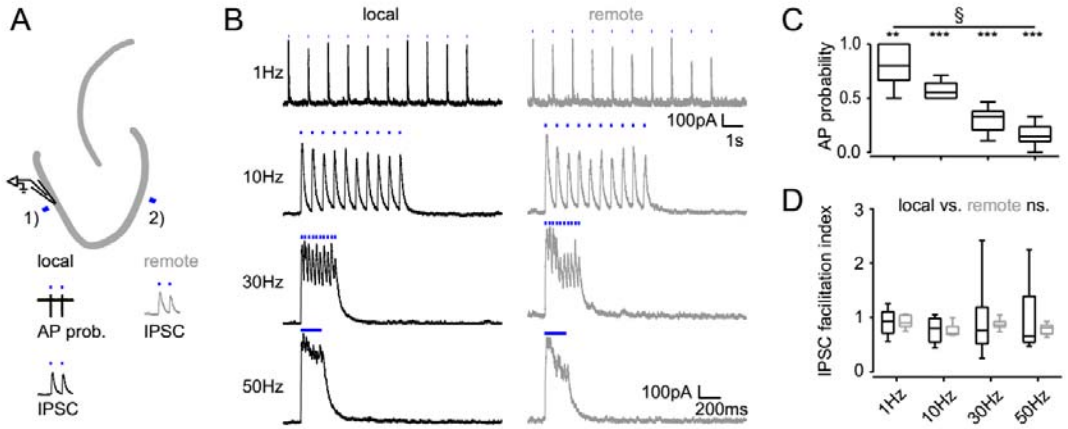

Fig. S5, Frequency dependence of feedback inhibition over space. Trains of 10 focal optic stimulations (20ms duration) were applied either locally (1) or remotely (2) to elicit feedback inhibition. **A)** Schematic of the experimental paradigm and example traces of elicited cell attached spikes or IPSCs. **B)** Example traces for stimulation at 1, 10, 30 Hz or continuously for 200 ms of a local or remote GC populations (black and grey, respectively). **C)** The AP probability index (mean probability during the last three pulses normalized to the first pulse (one-way RM ANOVA, P<.001 for frequency, Bonferroni corrected Wilcoxon signed rank test for deviation from 1; P=.024, =.008, =.008 and =.008 for 1Hz, 10Hz, 30Hz and continuous stimulation respectively). **D)** Facilitation indices of local (dark grey) and remote (light grey) stimulation (two-way RM ANOVA; P=.635, =.314 and =.687 for location, frequency and interaction respectively).

bioRxiv preprint doi: https://doi.org/10.1101/813188; this version posted October 21, 2019. The copyright holder for this preprint (which was not certified by peer review) is the author/funder, who has granted bioRxiv a license to display the preprint in perpetuity. It is made available under aCC-BY-NC 4.0 International license.

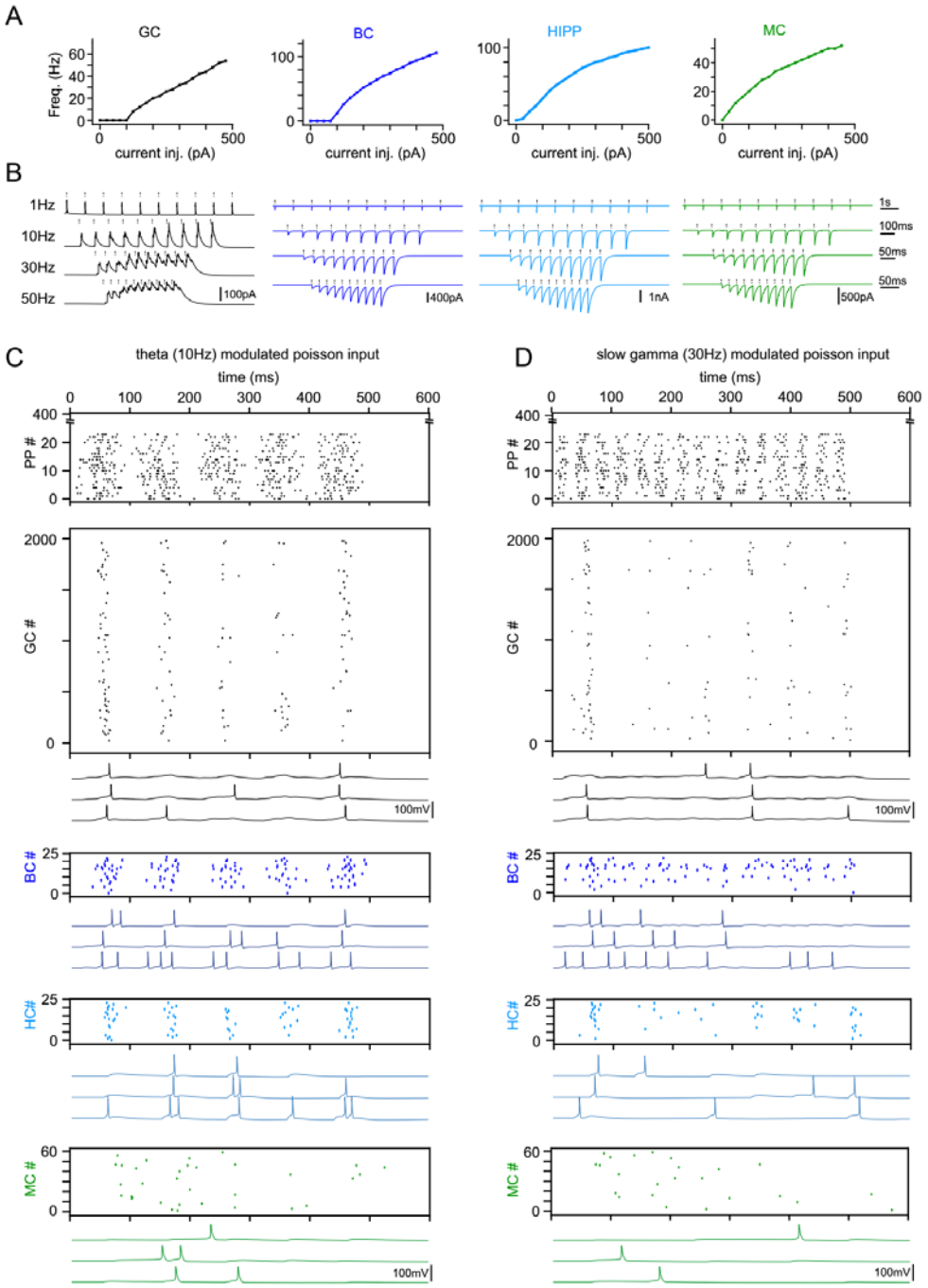

Fig. S6, Model Tuning and Validation. A) Frequency responses to somatic current injections of model celltypes (GC: granule cells, BC: basket cells, HC: hilar perforant path associated cells, MC: mossy cells). All model cells were matched to data by Santhakumar et al., (2005). **B)** Simulation of synchronous frequency stimulation of GCs and the resulting PSCs in modelled cell types, analogous to Fig. 4. **C)** Representative theta modulated PP input and population responses (scatterplots) of all modelled cell types. Following each scatterplot are three examples of spiking cells of the respective type. **D)** Same as (C) but for slow gamma modulated inputs.

bioRxiv preprint doi: https://doi.org/10.1101/813188; this version posted October 21, 2019. The copyright holder for this preprint (which was not certified by peer review) is the author/funder, who has granted bioRxiv a license to display the preprint in perpetuity. It is made available under aCC-BY-NC 4.0 International license.

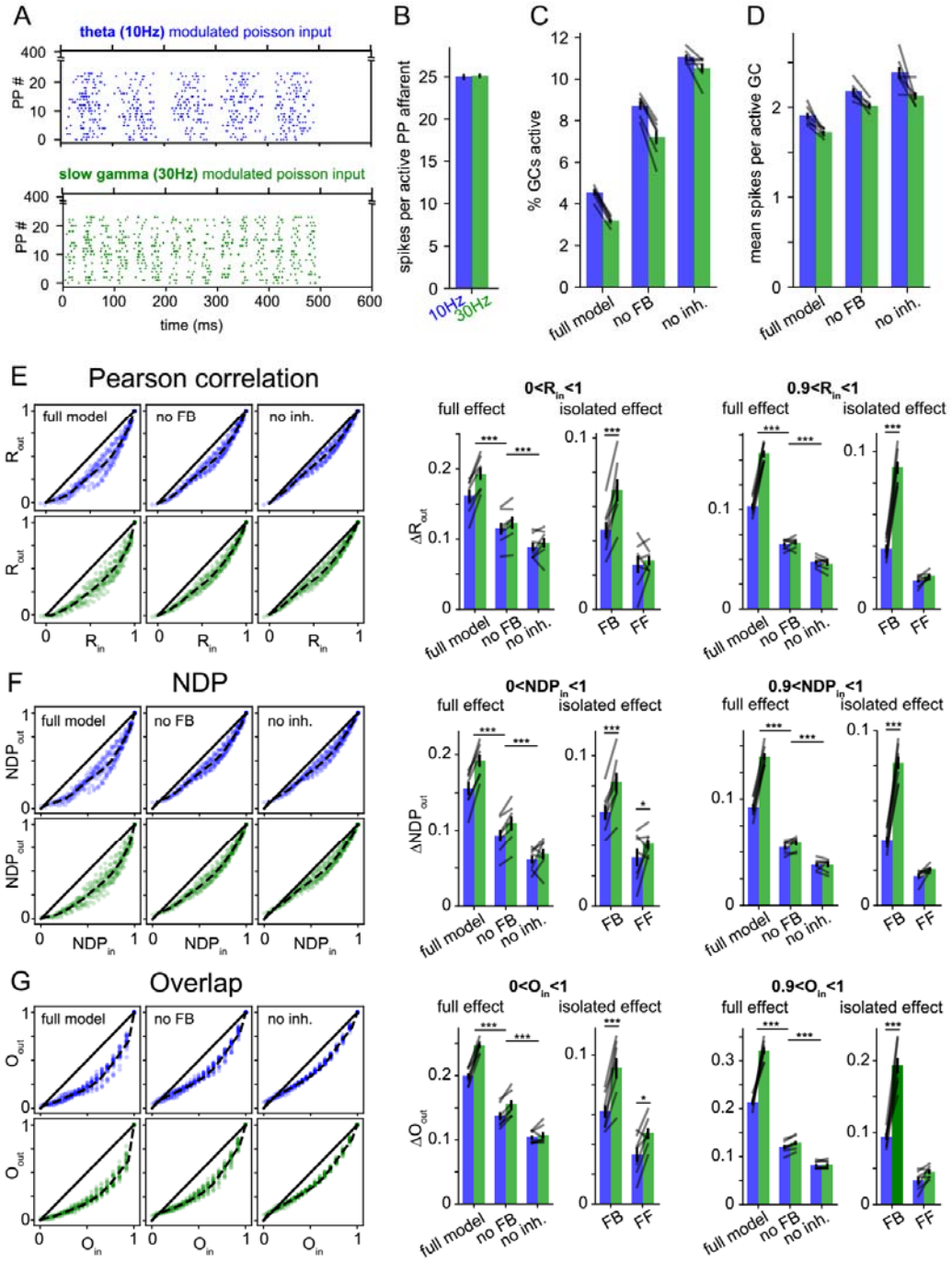

bioRxiv preprint doi: https://doi.org/10.1101/813188; this version posted October 21, 2019. The copyright holder for this preprint (which was not certified by peer review) is the author/funder, who has granted bioRxiv a license to display the preprint in perpetuity. It is made available under aCC-BY-NC 4.0 International license.

Fig. S7, Robustness over different Similarity Metrics, To test if the main finding of frequency dependent pattern separation, particularly for highly similar inputs, depended on the similarity metric used, the original data was reanalyzed with two alternative similarity metrics. As in the main figures data points in bar graphs represent the 7 independent network seeds. For each network (seed) we ran sets of patterns for the full model, a network without feedback inhibition (no FB) and a model with no inhibition (no inh.). **A)** Examples of the theta (10Hz) and gamma (30Hz) modulated perforant path (PP) input spike patterns. **B)** Mean number of APs per active PP afferent. **C)** Fraction of active GCs across the different conditions. **D)** Mean number of APs per active GC across conditions. **E)** Pearson's correlation coefficient R (as in Fig. 6) **left:** exemplary scatterplots of pattern separation effects. **right:** bargraphs of the mean pattern separation effect over the full input similarity range (0<Rin1) or only highly similar input patterns (0.9<R<1). Full effects measure the mean pattern separation effect for each network condition: full model, no feedback (no FB) and no inhibition (no inh.). Isolated effects measure the pattern separation contribution of individual circuit motifs: feedback inhibition (FB) and feedforward inhibition (FF). **F)** same as (E) but using normalized dot product (NDP) as similarity metric for input and output comparisons. **G)** Same as (E) but using population overlap as similarity metric. Overlap is defined as the number of cells active in both patterns (logical and) divided by the number of cells active in either pattern (logical or). The full effects were tested with 2x3 ANOVAs followed by Sidak's postests for differences between conditions. Isolated effects were tested with 2x2 ANOVAs followed by Tukey posttests for differences between frequencies. Asterisks indicate significance in posttests given significant overall effects (*P<.05,**P<0.01,***P<0.001).

bioRxiv preprint doi: https://doi.org/10.1101/813188; this version posted October 21, 2019. The copyright holder for this preprint (which was not certified by peer review) is the author/funder, who has granted bioRxiv a license to display the preprint in perpetuity. It is made available under aCC-BY-NC 4.0 International license.

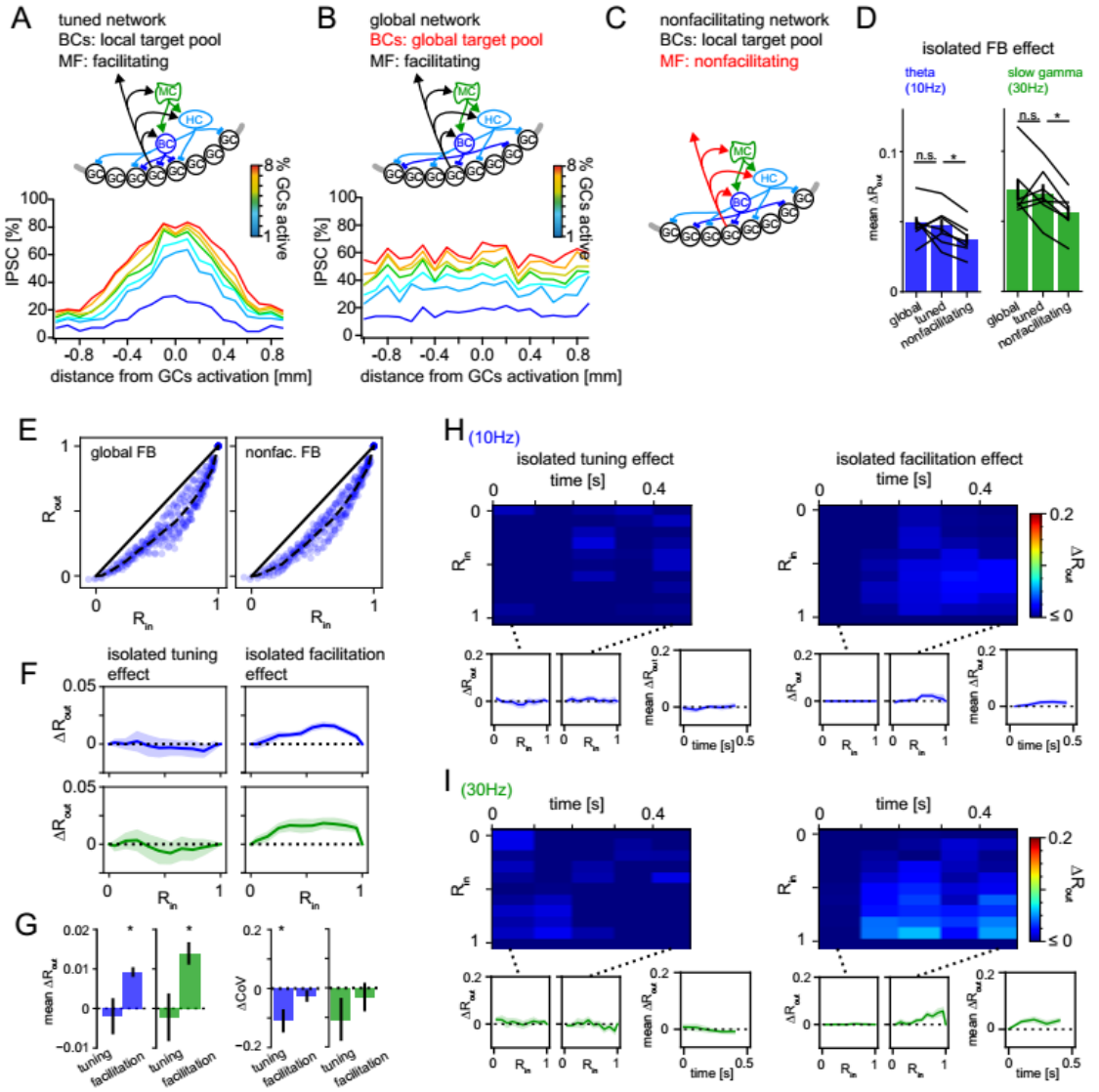

Fig. S8, Isolated pattern separation effects of spatial tuning and MF facilitation, Effects of isolated manipulations were computed for the DG model as in Fig 6. **A)** Schematic of the full tuned network and the resulting spatial profile of inhibition (as in Fig. 5). **B)** Schematic of the global network (with unrestricted BC target pool) and the resulting spatial profile of inhibition. **C)** Schematic of the non-facilitating network. **D)** Isolated mean feedback effects of the global, tuned and non-facilitating models. Two-way RM ANOVA showed: p<0.001, =0.020, =0.402 for frequency, condition and interaction respectively with * indicating significance in Dunnett's posttest against the full tuned effect. p=0.742 and 0.020 for global and non-facilitating, respectively at 10Hz; p=0.650 and 0.001 for global and non-facilitating, respectively at 30Hz. **E)** Exemplary pattern separation plots of theta modulated inputs when spatial tuning (left) or MF facilitation (right) was removed. **F)** Isolated pattern separation effects of the given manipulation for theta (blue) or gamma (green) modulated inputs as a function of input similarity. **G)** Isolated effect of the given manipulation on mean ΔR_{out} (left) and the coefficient of variance (ΔCoV) of pattern separation between individual comparisons (right). **H, I**) Time-resolved analyses of isolated effects of spatial tuning (left) and MF facilitation (right) for theta (top row) and slow gamma (bottom row) modulated inputs. In each subpanel the bottom left and middle insets show ΔR_{out} as a function of input similarity of the first and last time windows respectively. The bottom right insets show the evolution of the mean ΔR_{out} over time.

bioRxiv preprint doi: https://doi.org/10.1101/813188; this version posted October 21, 2019. The copyright holder for this preprint (which was not certified by peer review) is the author/funder, who has granted bioRxiv a license to display the preprint in perpetuity. It is made available under aCC-BY-NC 4.0 International license.

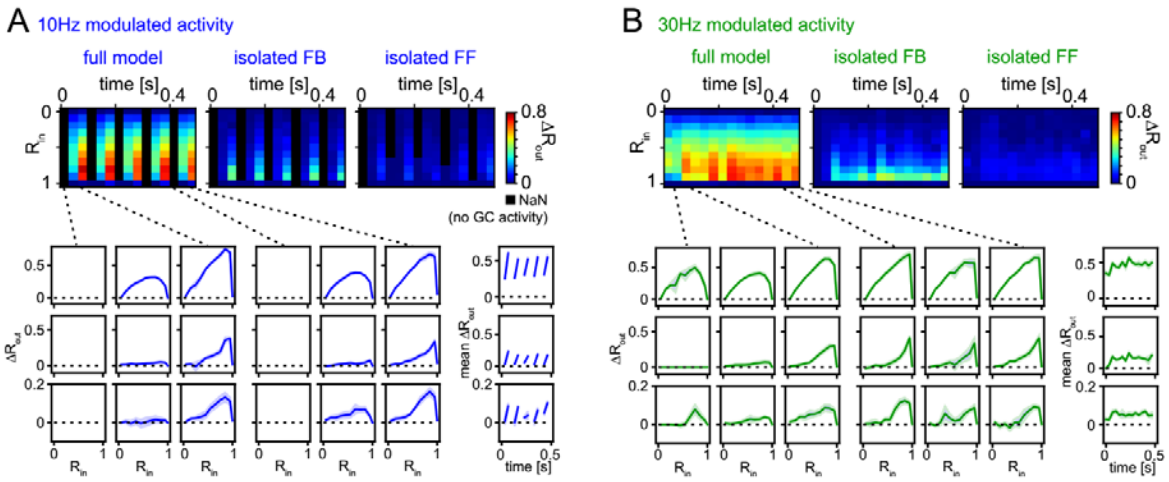

Fig. S9 Robustness for shorter analysis time-window, A). 33ms time-resolved pattern separation effects of the full model, isolated feedback (FB) or feedforward (FF) inhibition for theta modulated input (10Hz). All analyses were performed as above but with rate vector correlations computed for 33 ms time windows (instead of 100 ms or 600 ms, as in Fig.6). The bottom insets show ΔR_{out} as a function of input similarity for the first and last three time windows. The bottom right insets show the evolution of the mean ΔR_{out} over time. **B)** Same as (A) but for slow gamma (30Hz) modulated inputs. Data represent mean ± SEM of n=7 random network seeds.

bioRxiv preprint doi: https://doi.org/10.1101/813188; this version posted October 21, 2019. The copyright holder for this preprint (which was not certified by peer review) is the author/funder, who has granted bioRxiv a license to display the preprint in perpetuity. It is made available under aCC-BY-NC 4.0 International license.

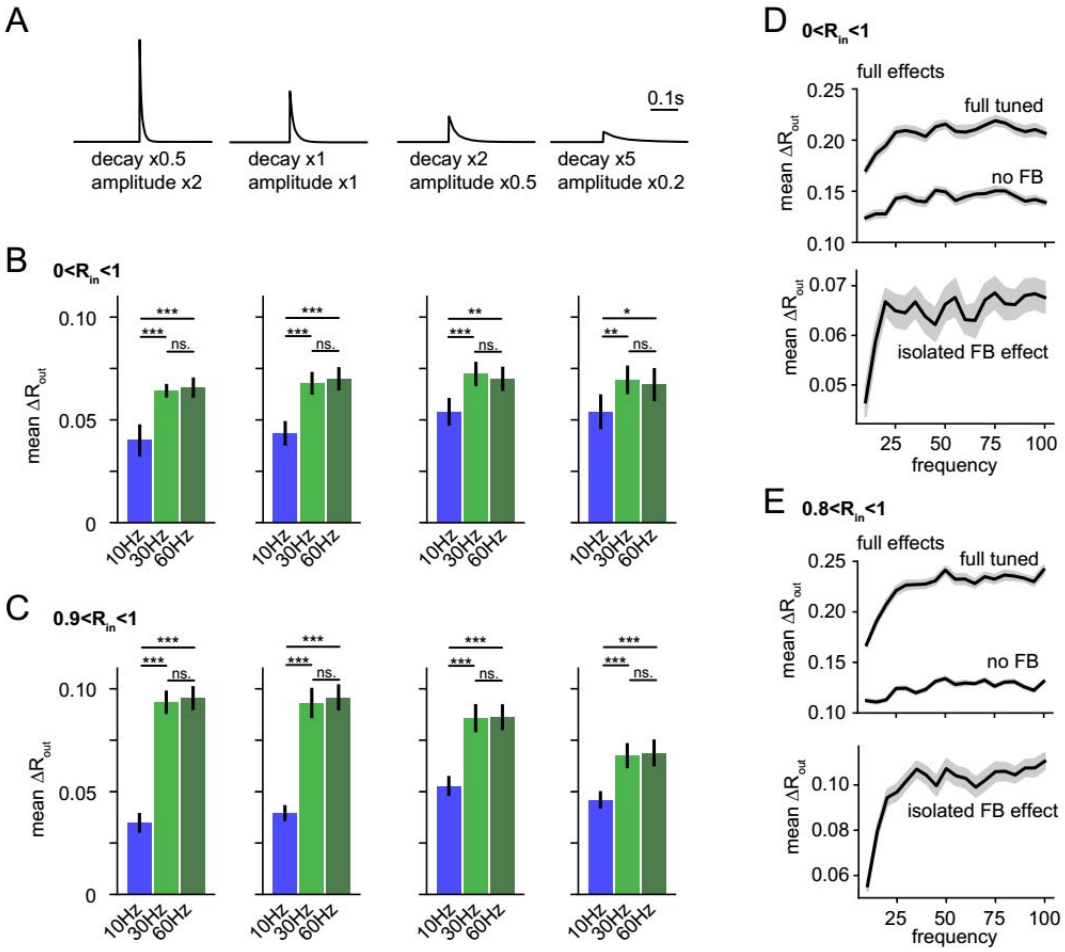

Fig. S10, Robustness over various IPSC decay time-constants and over the full gamma range, A-C) To test if the frequency dependence of feedback inhibitory pattern separation remained robust for different IPSC decay time constants we probed a range of altered time constants (our experimentally matched time constant x0.5, x1, x2 and x5) while maintaining total inhibitory conductance in the network constant by complementary adjustment of IPSC amplitude. As we expected a potential interaction between IPSC decay and modulation frequency, we probed model runs for each factor with 10Hz, 30Hz and 60Hz modulation. The isolated feedback inhibitory effects were computed and impacts of decay and frequency were examined with 4x3 ANOVAs followed by Tukey posttests for differences between frequencies. Asterisks indicate significance in posttests given significant overall effects (*P<.05,**P<0.01,***P<0.001).**A)** Illustration of modified IPSC time-courses. **B)** Mean pattern separation effect of isolated feedback inhibition over the full input similarity range ($0<R_{in}<1$). **C)** Same as (B) but only for highly similar input patterns. Analyses in A-C were performed on 7 new network seeds with simulation and analysis otherwise identical to Fig.6. **D-E)** To probe the robustness of frequency dependent feedback inhibitory pattern separation over an even larger range of frequency modulation we next simulated the effects over a range from 10 to 100Hz in 5Hz steps. To provide computational tractability we performed only 8 runs per frequency (instead of 24 runs as in all other simulations) leading to fewer pattern comparisons, and somewhat noisier readouts. For the majority of frequencies, no input comparisons with R>0.9 occurred so we defined ($0.8<R_{in}<1$) as highly similar input patterns, potentially leading to a slight underestimation of our effects.

bioRxiv preprint doi: https://doi.org/10.1101/813188; this version posted October 21, 2019. The copyright holder for this preprint (which was not certified by peer review) is the author/funder, who has granted bioRxiv a license to display the preprint in perpetuity. It is made available under aCC-BY-NC 4.0 International license.

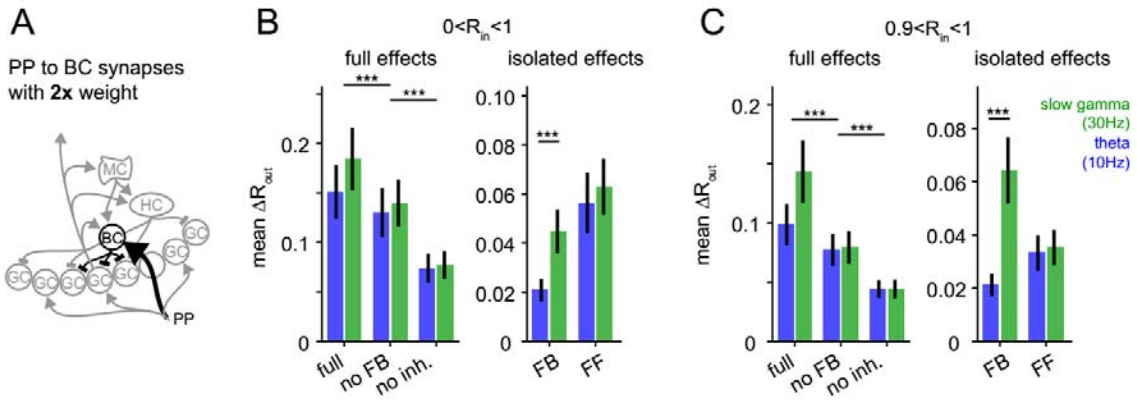

Fig. S11, Robustness for increased feedforward inhibition, To test if the frequency dependent enhancement of feedback inhibitory pattern separation of highly similar inputs was sensitive to the changes in the relative strengths of feedforward and feedback inhibition, we increased the perforant path (PP) to basket cell (BC) synapse weight 2x. **A)** Illustration of the network alteration. **B)** The resulting full pattern separation effects (left) and isolated feedback (FB) and feedforward (FF) effects (right) as mean over all input similarities. **C)** Same as (B) but only for highly similar input patters. Full effects were tested with 2x3 ANOVAs followed by Sidak's postests for differences between conditions. Isolated effects were tested with 2x2 ANOVAs followed by Tukey posttests for differences between frequencies. Asterisks indicate significance in posttests given significant overall effects (*P<.05,**P<0.01,***P<0.001).

	From	To	IN location	Method	Freq.	short term dynamics	pulses	species	Authors	
GC to IN	GC	BC	GC-border	dual patch	50 Hz	PPD	2	juv. wistar rats	Geiger and Jonas (1997)	
	GC	BC	not stated	dual patch	20 & 50 Hz	depression	10 & 5	C57/BL6 mice	Espinoza et al. (2019)	
	GC	SST	not stated	dual patch	20 Hz	facilitation	10	C57/BL6 mice	Espinoza et al. (2019)	
e-stim to IN	PP & C/A	FS	GC-border	e-stim/ spike prob.	50 Hz	decreased spike prob.	10	juv. SD rats	Liu et al. (2014)	q
	PP	FS	GC-border	e-stim	10 Hz	depression to 40%	20	juv. C57/BL6 mice	Ewell and Jones (2010)	q
	PP & C/A	non-FS	GC-border	e-stim/ spike prob.	50 Hz	increased spike prob.	10	juv. SD rats	Liu et al. (2014)	q
	PP & MF	FS	GC-border	e-stim	30 Hz	facilitation		juv. wistar rats	Sambandan et al. (2010)	
	MF	FS	GC-border	e-stim (close)	30 Hz	facilitation, PPF		juv. wistar rats	Dasgupta et al (2015)	
e-stim to MC	MF	MC	Hilus	e-stim	20 Hz	facilitation to 500%	5	juv. wistar rat	Lysetskiy (2005)	q
IN to GC	BC	GC	GC-border	dual patch	10 & 50 Hz	depression to ~25% & 0%	> 850	juv. wistar rats	Kraushaar and Jonas (2000)	q
	CCK & PV	GC	GC-border	dual patch	50 Hz	depression to 20%	10	juv. wistar rats	Hefft and Jonas (2005)	q
	SST	GC	Hilus	dual patch	50 Hz	depression to 20%	20	adult GIN mice	Zhang et al. (2009)	q
	BC	GC	GC-border	dual patch	20 Hz	PPD to 39%	2	juv. C57/BL6 mice	Bartos et al. (2002)	q
	FS	GC	GC-border	dual patch	10 Hz	PPD to 85%	2	juv. SD rats	Harney and Jones (2002)	q
	non-FS	GC	GC-border	dual patch	10 Hz	PPD to 77 %	2	juv. SD rats	Harney and Jones (2002)	q
	PP	GC	GC-border	e-stim	10 Hz	depression to 40%	20	juv. C57/BL6 mice	Ewell and Jones (2010)	q
	FS	GC	GC-border	dual patch	25 Hz	depression	5	juv. SD rats	Liu et al. (2014)	
	non-FS	GC	GC-border	dual patch	25 Hz	facilitation	5	juv. SD rats	Liu et al. (2014)	
	CCK	GC	not stated	dual patch	20 Hz	depression	10	C57/BL6 mice	Espinoza et al. (2019)	
IN to IN	BC	BC	GC-border	dual patch	50 Hz	depression to 50%	10	juv. wistar rats	Savanthrapadian et al. (2014)	q
	HICAP	HICAP	GC-border	dual patch	50 Hz	facilitation to 160%	10	juv. wistar rats	Savanthrapadian et al. (2014)	q
	HIPP	HIPP	GC-border	dual patch	50 Hz	facilitative envelope	10	juv. wistar rats	Savanthrapadian et al. (2014)	q
	HICAP	BC	GC-border	dual patch	50 Hz	no change	10	juv. wistar rats	Savanthrapadian et al. (2014)	q
	HIPP	BC	GC-border	dual patch	50 Hz	no change	10	juv. wistar rats	Savanthrapadian et al. (2014)	q
	BC	BC	GC-border	dual patch	20 Hz	PPD to 26%	2	juv. C57/BL6 mice	Bartos et al. (2002)	q
	TML (non-FS)	TML	GC-border	dual patch	50 Hz	facilitation , PPF to ~220%	8	adult wistar rats	Yu et al. (2015)	
	IN	IN	Hilus	dual patch	20 Hz	PPD to ~80%	2	juv. SD rats	Larimer and Strowbridge (2008)	q
MC	IN	MC	Hilus	dual patch	20 Hz	PPD to ~80%	2	juv. SD rats	Larimer and Strowbridge (2008)	q
	MC	IN / MC	Hilus	dual patch	20 Hz	no change	2	juv. SD rats	Larimer and Strowbridge (2008)	q

cells	
BC	basket cell
CCK	cholecystokinin expressing cell
FS	fast spiking cell (> 50Hz peak firing frequency)
GC	granule cell
HICAP	hilar commissural/associational path associated cell
HIPP	hilar perforanth path associated cell
IN	not further categorized interneuron
MC	mossy cell
non- FS	non- FS (< 50Hz peak firing frequency)
SST	somatostatin expressing cell
TML	total molecular layer cell

other	
blue	depression, quantitatively described
green	facilitation, quantitatively described
PPD	paired pulse depression
PPF	paired pulse facilitation
e- stim	extracellular electrical stimulation
C/A	commissural/ associational
MF	mossy fiber
PP	perforant path
SD rat	spraque dawley rat
juv.	juvenile (12 to 25 days postnatally)
q	quantitatively described

bioRxiv preprint doi: https://doi.org/10.1101/813188; this version posted October 21, 2019. The copyright holder for this preprint (which was not certified by peer review) is the author/funder, who has granted bioRxiv a license to display the preprint in perpetuity. It is made available under aCC-BY-NC 4.0 International license.

Supplementary Table 1, Literature review for DG circuit short term dynamics, Studies reporting short term dynamics within the DG circuit were reviewed with a main focus on facilitation or depression of synaptic connections defined by pre and postsynaptic cell types. Note the abundance of depressing synapses (quantitative descriptions of depression blue). Also note the complexity of direct connections between Interneurons (lower third of the table).

bioRxiv preprint doi: https://doi.org/10.1101/813188; this version posted October 21, 2019. The copyright holder for this preprint (which was not certified by peer review) is the author/funder, who has granted bioRxiv a license to display the preprint in perpetuity. It is made available under aCC-BY-NC 4.0 International license.

To

From

	GC, 2000	MC, 60	BC, 24	HC, 24
PP				
Weight (nS)	1	/	1 (2)	/
Decay Tau (ms)	10		6.3	
Facilit. Tau (ms)	0		0	
Delay (ms)	0		0	
Target pool	2000		24	
Divergence	100		1 BC/PP	
Target segments	mid. dendrite		distal dend	
GC				
Weight (nS)	/	2	2.5	2.5
Facilitation Max.		10x	10x	10x
Decay Tau (ms)		7.6	8.7	8.7
Facilit. Tau (ms)		500	500	500
Delay (ms)		1.5	0.8	1.5
Target pool		12	8	24
Divergence		1:1	1:1	1:1
Target Segments		prox. dendrite	prox. dendrite	prox. dendrite
MC				
Weight (nS)	/	0.5	0.3	0.2
Decay Tau (ms)		2.2	2	6.2
Facilit. Tau (ms)		0	0	0
Delay (ms)		2	3	3
Target pool		24	12	20
Divergence		1:3	1:1	1:2
Target segments		prox. dendrite	prox. dendrite	mid. dendrite
BC				
Weight (nS)	1.2	1.5	7.6	/
Decay Tau (ms)	20 (10, 40, 100)	3.3	1.8	
Facilit. Tau (ms)	0	0	0	
Delay (ms)	0.85	1.5	0.8	
Target pool	560	28	12	
Divergence	1:400	1:3	1:2	
Target segments	soma	prox. dendrite	prox. dendrite	
HC				
Weight (nS)	6	1.5	0.5	/
Decay Tau (ms)	20 (10, 40, 100)	6	5.8	
Facilit. Tau (ms)	0	0	0	
Delay (ms)	3.8	1	1.6	
Target pool	2000	60	24	
Divergence	1:640	1:4	1:4	
Target segments	distal dend	mid dendrite 1, 2	distal dend	

bioRxiv preprint doi: https://doi.org/10.1101/813188; this version posted October 21, 2019. The copyright holder for this preprint (which was not certified by peer review) is the author/funder, who has granted bioRxiv a license to display the preprint in perpetuity. It is made available under aCC-BY-NC 4.0 International license.

Supplementary Table 2, Model Parameters, Overview of synaptic and intrinsic parameters between model cell-types. First row includes modeled cell number per type. **PP**: perforant path, **GC**: granule cell, **MC**: mossy cell, **BC**: basket cell, **HC**: Hilar perforant path associated cell; Weight: maximal synaptic conductance, Facilitation Max.: maximal fold increase of synaptic conductance, Decay Tau: synaptic decay time constant, Facilit. Tau: facilitation time constant, Delay: latency to postsynaptic event after presynaptic action potential, Target pool: range of n closest cells potentially receiving an output, Divergence: number of output synapses per cell stochastically picked from target pool, Target segments: cellular compartment receiving the synapse. Values in brackets are values for robustness analyses in Figs. S10, S11.